CHALMERS

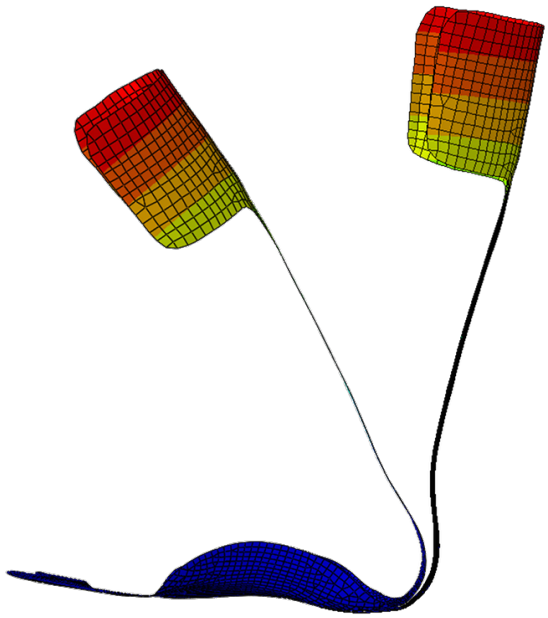

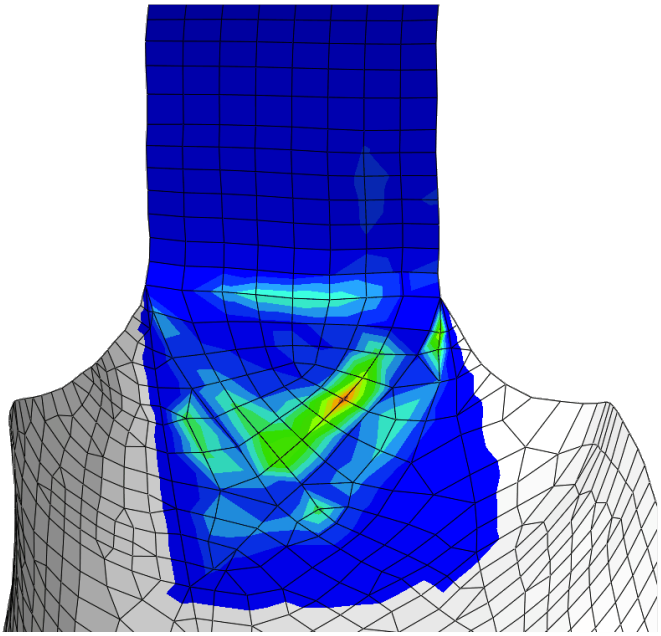

Composites failure modeling and optimization of a spring orthosis

Master's thesis in Solid and Fluid Mechanics

LINN SVÄRD

Department of Applied Mechanics
Division of Material and Computational Mechanics
CHALMERS UNIVERSITY OF TECHNOLOGY
Gothenburg, Sweden 2012
Master's thesis 2012:19

MASTER'S THESIS IN SOLID AND FLUID MECHANICS

Composites failure modeling and optimization of a spring orthosis

LINN SVÄRD

Department of Applied Mechanics
Division of Material and Computational Mechanics
CHALMERS UNIVERSITY OF TECHNOLOGY

Gothenburg, Sweden 2012

Composites failure modeling and optimization of a spring orthosis

LINN SVÄRD

Master's thesis 2012:19
ISSN 1652-8557
Department of Applied Mechanics
Division of Material and Computational Mechanics
Chalmers University of Technology
SE-412 96 Gothenburg
Sweden
Telephone: +46 (0)31-772 1000

Cover:
LHS: Deflection of the spring orthosis. RHS:Delamination initiation in the heel of the orthosis.

Chalmers Reproservice
Gothenburg, Sweden 2012

Composites failure modeling and optimization of a spring orthosis

Master's thesis in Solid and Fluid Mechanics
LINN SVÄRD
Department of Applied Mechanics
Division of Material and Computational Mechanics
Chalmers University of Technology

Abstract

This thesis work deals with failure modeling of composite materials. The main objective of the thesis is to acquire a general understanding of how to model delamination in composites. This modeling technology is then applied to a problem of delaminations in a spring orthosis, which is an orthopedic device that supports the lower leg and foot. At the department of orthopedic technology at Borås Hospital delaminations in the heel area of the orthosis have been noticed and the goal with the thesis work is to investigate the influence of the lay-up on the performance of the orthosis.

The thesis work is divided into three parts. In order to investigate how to best model delamination, benchmark tests were studied. The modeling of the delamination was done using the cohesive zone method. To be able to verify the material model of the carbon-fibre epoxy composite used in the orthosis a simulation was made of a four-point bending test. The methodology developed in these analyses was used when modeling the orthosis. The modeling was performed in Abaqus CAE and Composites Modeler was used to define the ply lay-ups and the draping of the orthosis. An optimization study was performed using HyperStudy in order to improve the delamination performance of the orthosis by varying the fiber angles of the different plies.

The results from the modeling of the benchmark tests agreed very well with the theoretical and experimental values. For the four point bending test the modeling results were also in good agreement with test results. The modeling did not capture the delaminations in the test specimens, although, the load which caused failure of the first ply and also ultimate failure was predicted with good agreement. The optimization study resulted in a lay-up with only slightly improved results compared with the original lay-up. However, the optimization study gave some knowledge of how the different ply angles affect the behavior of the orthosis regarding stiffness and failure behavior.

Keywords: Abaqus CAE, Carbon fiber, Cohesive Zone, Composite, Delamination, Failure, Finite Element Modeling, Four-point bending, Optimization, Ply stacking sequence, Spring Orthosis, Tsai-Wu

Preface

This report covers finite element analysis of a carbon fiber spring orthosis. It is a Master's Thesis for the degree Master of Science in Solid and Fluid Mechanics at Chalmers University of Technology. The work has been carried out at FS Dynamics in Gothenburg in collaboration with the department of orthopedic technology at Borås Hospital during summer and autumn of 2011.

Acknowledgements

First and foremost I would like to thank my supervisor at FS Dynamics, Rickard Juntikka, for your patient guidance and great help during this thesis work. I would also like to thank my supervisor and examiner at Chalmers, Prof. Magnus Ekh, for your support. Moreover, thanks goes to the staff at Ortopedteknik at Borås Hospital for taking the time and providing me with input.

Finally I would like to thank David. Even though you often distracted me from work, you deserve a big thank you for your support.

Gothenburg, February 2012
Linn Svärd

Nomenclature

Roman letters

a	Crack length
B	Specimen width
D	Damage variable
E	Stiffness (Young's) modulus
F	Tsai-Wu failure coefficients
G	Strain energy release rate
G_C	Critical strain energy release rate
h	Half thickness of specimen
I	Area moment of inertia
P	Applied load
v	Volume fraction

Greek letters

α	Mixed mode parameter in the power law failure criterion
δ	Displacement
ε_i	The i:th strain component
$\varepsilon_{c,t}$	Compressive/tensile failure strains
η	Mixed mode parameter in the BK-criterion
γ_{12}	In-plane shear failure strain
ν_{12}	In-plane Poisson's ratio
ν_{23}	Transverse Poisson's ratio
ξ	Empirical constant in the Halpin-Tsai equation
σ_i	The i:th stress component
$\sigma_{c,t}$	Compressive/tensile strength
τ_{12}	In-plane shear strength
τ_{23}	Inter-laminar shear strength

Subscripts

c	compressive
f	fiber
m	matrix
t	tensile

Abbreviations

ARSM	Adaptive Response Surface Method
4PB	Four-point bending
BK	Benzeggagh-Kenan
DCB	Double cantilever beam
DOE	Design of Experiment
ENF	End notched flexure
FRMM	Fixed ratio mixed mode
ILSS	Inter-laminar shear strength

Contents

1 Introduction

This chapter gives the background to this thesis work and describes the purpose and aim of it. The methodology and the limitations of the performed work are also presented. At the end of this chapter the outline of the thesis is described.

1.1 Background

The use of carbon fibre composites has increased drastically in recent years. One field of application is in orthopedic technology where it is used to build specially adapted aids such as orthoses. Generally, an orthosis is defined as *"an externally applied device used to modify the structural or functional characteristics of the neuro-muscular system"* [1]. One of the most advanced types is the carbon fiber spring orthosis which supports the lower leg and the foot, see Figure 1.1.1. Spring orthoses are mainly worn by people with crouch gait, i.e. a walking pattern characterized by excessive knee flexion during stance phase. The majority of these people are children suffering from myelomeningocele.

(a) *A pair of spring orthoses with buckles.*

(b) *The analyzed orthosis with all exteriors removed.*

Figure 1.1.1: *The spring orthosis.*

The department of orthopedic technology at Borås Hospital in Sweden manufactures approximately 30 - 35 of this type of spring orthosis each year. The orthoses are made by hand and the design is adapted for each patient. As the situation is today, there exists no consistent method of how to build the orthoses. It is the constructing engineers' judgement and experience of previously built orthoses that decides the appearance of new ones. This implies that the design of the orthoses can vary a lot from time to time and also depending on which engineer is constructing it.

To study and improve the performance of the orthoses built at Borås Hospital a Master's thesis work was performed during spring of 2010, cf. [2]. In this previous thesis work FE-analysis was used to study the stresses and deformations in the orthosis. Failure due to delamination was never considered. Delamination is an interlaminar failure which results in separation of the layers and is, according to the orthopedic engineers at Borås Hospital, the main reason that orthoses break. In Figure 1.1.2 delamination cracks in a broken orthosis are illustrated. The delamination occurs in the curved heel area which is the most critical section for failure according to the engineers at Borås Hospital.

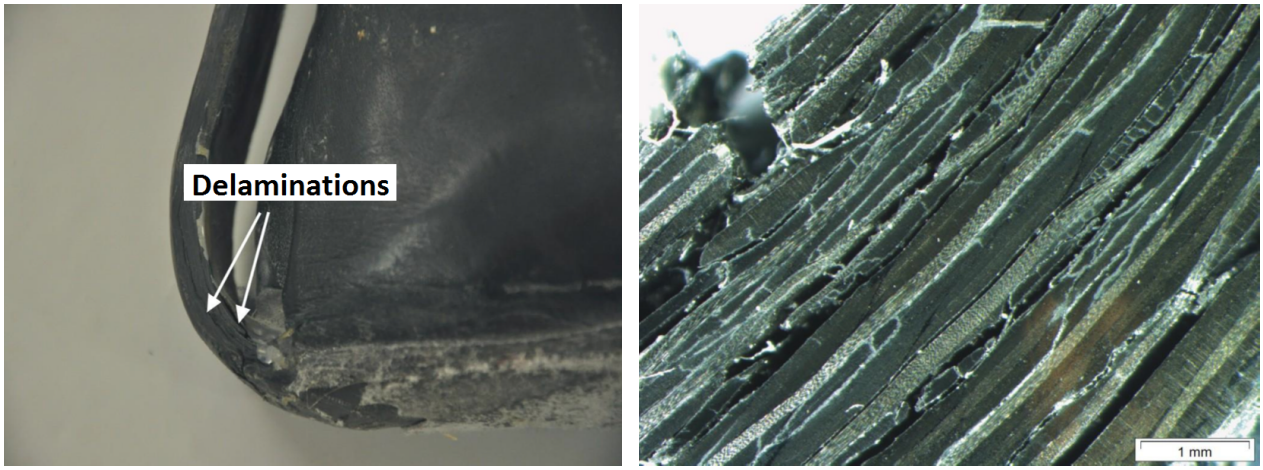

(a) *Delaminations observed in the curved heel section.* (b) *Microscopic picture of the curved section.*

Figure 1.1.2: *Delamination cracks in the spring orthosis. [3]*

1.2 Objective

The main objective of this thesis is to optimize the delamination failure performance of the orthosis. In particular it is desired to minimize the delaminations in the heel area since this have been identified as a problem. The thesis work also serves to get a general understanding of how to model delamination in composites.

1.3 Limitations

The optimization is limited to study how the ply orientations affect the failure behavior of the orthosis. The number of plies in the different parts of the orthosis is never changed and the same draping pattern is used as in previous thesis work. The geometry and the material of the orthosis are also kept constant through all the simulations.

1.4 Method

Firstly, three different benchmark tests were studied in order to investigate how to best model delamination. Then, to be able to verify the material model of the composite used in the orthosis, a simulation was made of a four-point bending test conducted by SP Technical Research Institute of Sweden. The methodology developed in these analyses was then used in the modeling of the orthosis. Finally, an optimization study was performed in order to improve the delamination performance of the orthosis.

All the FEM-simulations were performed in Abaqus/CAE (v6.11). To create composite layups the Composites Modeler plug-in was used. The optimization was conducted using HyperStudy.

The cleaned up geometry of the scanned orthosis from previous thesis work was used in the study. This geometry was re-meshed using the pre-processor ANSA to better suit the analyses performed in this thesis work.

1.5 Thesis outline

The thesis is organized as follows. In Chapter 2 the theory is introduced, this involves a description of composites (background, failure modes and delamination) and the used optimization method. Chapter 3 describes the different parts of the method for the work: the delamination modeling, the four point bending test and the modeling and optimization of the orthosis. In Chapter 4 the results are presented. Chapter 5 contains the conclusions and a discussion. Chapter 6 ends the thesis by giving some recommendations for future work.

2 Theory

In this section the theory behind the work in this thesis is presented. First, a general background to composites including some information about their different failure modes and micro-mechanics is introduced. This is followed by a more detailed description of delamination. Finally, the theory behind the optimization method is presented.

2.1 General introduction to composite materials

A composite material is a combination of two or more materials with significantly different physical and/or chemical properties. The properties of a composite are mostly very different from the properties of the single components. A composite contains a reinforcement material which is surrounded by a matrix material. The matrix material supports the reinforcement and gives the composite its shape. Load subjected to the matrix is transferred to the reinforcement, which purpose is to improve stiffness, strength and toughness of the composite. The mechanical properties of the composite is to a large extent depending on the configuration (the typology) of the reinforcement constituent. In a fibrous reinforcement the aspect ratio of the fibers is an important factor. The aspect ratio is defined as the ratio between the length and the width of the cross section of the fibers. If the composite contains long fibers with a high aspect ratio it is classified as continuous, and if the fibers are short with low aspect ratios it is defined as discontinuous. Another important factor is the orientations of the fibers, they can either be aligned or randomly oriented. Continuous aligned fibers can for example be unidirectional or bi-directional (woven). An illustration of different composite typologies are shown in Figure 2.1.1.

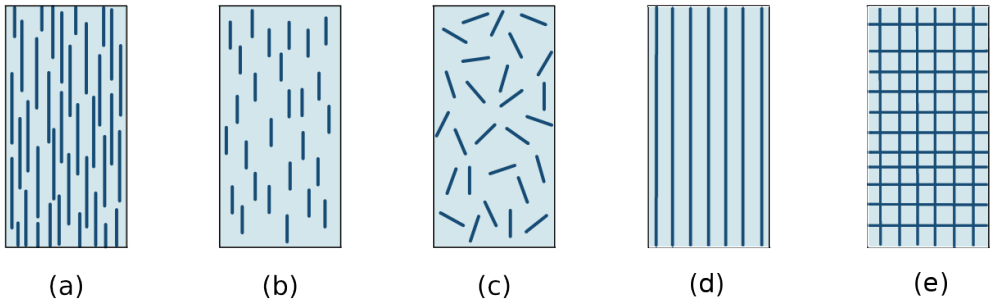

Figure 2.1.1: *Different typologies (acc. to [4]) of fibre-reinforced composite materials: a) continuous aligned b) discontinuous aligned c) discontinuous random-oriented d) continuous aligned, unidirectional (e) continuous aligned, woven.*

A composite often consists of many superimposed layers bonded together with the matrix material. Many layers, normally called plies or laminas, form a laminate as illustrated in Figure 2.1.2. To attain certain properties of the laminate it is common to have the fiber orientation change from ply to ply, cf. [5].

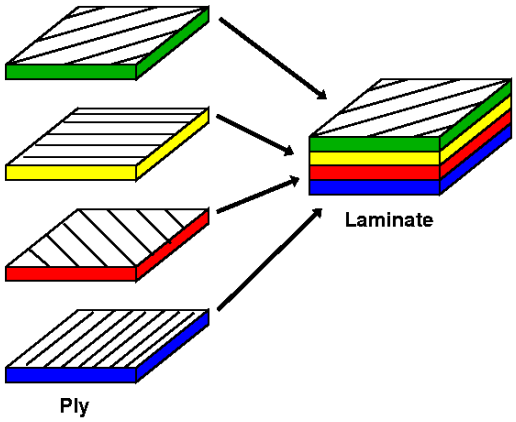

Figure 2.1.2: *A laminate is usually stacked with plies of different orientations.*

2.2 Micro-mechanics

When a composite material is analyzed on the level of the individual constituents, the term micro-mechanics is used. Given the material properties of the individual constituents micro-mechanics serves to predict the macroscopic behavior of the heterogeneous material with, in this case, transverse isotropy. In micro-mechanics the material properties are often estimated using different homogenization methods such as the rule-of-mixture and the Halpin-Tsai equation.

If E_f and E_m are the stiffnesses for the fiber and matrix materials, respectively, the rule of mixture for the longitudinal stiffness modulus (i.e. the stiffness in the fibre direction) is given by

$$E_1 = E_f v_f + E_m v_m \tag{2.2.1}$$

where v_f and v_m are the volume fractions for the fiber and matrix phase, respectively. For the in-plane Poisson's ratio the rule of mixture gives

$$\nu_{12} = \nu_f v_f + \nu_m v_m \tag{2.2.2}$$

where ν_f and ν_m are the Poisson's ratio for the fiber and matrix material, respectively.

For the parameters above the, rule of mixture gives in general well estimated results. For the transverse modulus and the shear modulus the results are in general less accurate. For these values the Halpin-Tsai equation is normally used.

The Halpin-Tsai equation for the transverse stiffness modulus is defined as

$$\frac{E_2}{E_m} = \frac{1 + \xi\eta v_f}{1 - \eta v_f} \qquad \text{where} \quad \eta = \frac{E_f - E_m}{E_f + \xi E_f} \tag{2.2.3}$$

where ξ is an empirical constant. The shear modulus G_{12} and the transverse shear modulus G_{23} are calculated the same way as E_2 by simply substituting E_f and E_m by G_f and G_m, respectively. The empirical constant ξ for E_2, G_{12} and G_{23} are determined by curve-fitting to experiments.

The transverse Poisson's ratio can then be determined by the following equation

$$\nu_{23} = \frac{E_2}{2G_{23}} - 1. \tag{2.2.4}$$

2.3 Failure of composites

Speaking of composites the term *failure* normally reflects the fact that the material fractures by a sequence of failure events rather than fracture due to a distinct stress or strain. There are several different ways for which the failure in a laminate can occur. Figure 2.3.1 shows the three general failure mechanisms; matrix cracks, fibre fracture and delamination. However, the failure mechanisms can also be divided into more complex states for both the fibers, matrix and interface including for example fiber micro-buckling.

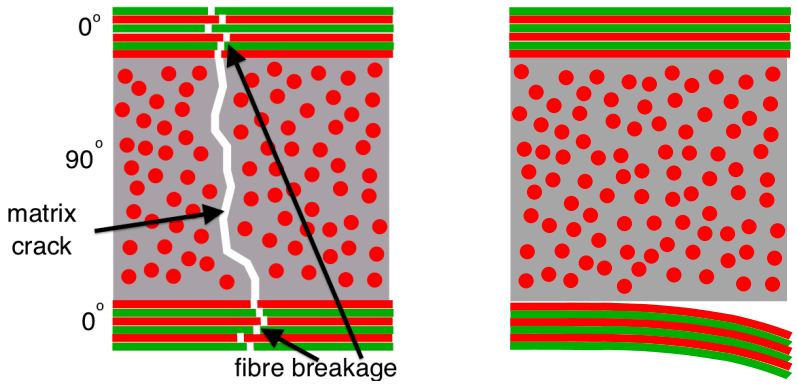

(a) *Matrix crack and fiber breakage.* (b) *Delamination.*

Figure 2.3.1: *Composite failure mechanisms.*

2.4 Failure criteria

To estimate when failure in a lamina occurs there exists several failure criteria of varying type and complexity. However, no criterion is perfectly able to predict failure accurately for all materials and load cases. As mentioned before the failure process is normally not trivial and micro-mechanical failure mechanisms such as fiber pullout, fiber bridging and fiber micro-buckling are not considered in the available theories. These approaches also neglect the existence and growth of cracks and other defects in the material. To take these failure mechanisms into account a fracture mechanical approach is needed, cf. [2]

In this section descriptions of some of the failure criteria that are most widely used are presented. From here on the subscripts 1 and 2 denotes the material direction, where the 1-direction is aligned with the fibers and the 2-direction is transverse to the fibers. The criteria described below are based on the assumption of plane stress in the lamina. The stresses and strains are denoted in Voigt notation where the subscript 6 stands for the first shear direction. The subscripts t and c represent tension and compression, respectively. It should be noted that both the tensile and compressive values are defined as positive in all of the following equations.

The two simplest failure criteria are the maximum stress criterion and maximum strain criterion. The **maximum stress criterion** assumes that failure occurs when any of the stresses are outside the interval for the corresponding strength. This can be defined as, cf. [6]

$$\begin{cases} -\sigma_{1c} < \sigma_1 < \sigma_{1t} \\ -\sigma_{2c} < \sigma_2 < \sigma_{2t} \\ |\sigma_6| < \tau_{12}. \end{cases} \tag{2.4.1}$$

where σ_{1c}, σ_{1t}, σ_{2c}, σ_{2t} are the compressive and tensile strength in the fiber direction and transverse direction, respectively, and τ_{12} is the shear strength.

Similarly the **maximum strain criterion** states that the material do not fail if the following relations are satisfied

$$\begin{cases} -\varepsilon_{1c} < \varepsilon_1 < \varepsilon_{1t} \\ -\varepsilon_{2c} < \varepsilon_2 < \varepsilon_{2t} \\ |\varepsilon_6| < \gamma_{12}. \end{cases} \tag{2.4.2}$$

The variables ε_{1c}, ε_{1t}, ε_{2c}, ε_{2t} and γ_{12} represent the failure strains denoted the same way as the failure stresses.

These two failure criteria are non-interactive which means that they do not take the interaction between the different stress components into account. Examples of two interactive failure criteria are the Tsai-Hill criterion and the Tsai-Wu criterion. They are both quadratic criteria, the former is sometimes referred to as the "von Mises for composites". The Tsai-Wu failure criterion is a bit more general than the Tsai-Hill criterion since it considers different strengths in compression and tension. The **Tsai-Wu failure criterion** is given by, cf. [6]

$$F_1\sigma_1 + F_2\sigma_2 + F_{11}\sigma_1^2 + F_{22}\sigma_2^2 + F_{66}\sigma_6^2 + 2F_{12}\sigma_1\sigma_2 = 1 \tag{2.4.3}$$

The coefficients in equation 2.4.3 are defined in terms of the different strengths as follows

$$F_1 = \frac{1}{\sigma_{1t}} - \frac{1}{\sigma_{1c}}; \quad F_2 = \frac{1}{\sigma_{2t}} - \frac{1}{\sigma_{2c}}; \quad F_{11} = \frac{1}{\sigma_{1t}\sigma_{1c}}; \quad F_{22} = \frac{1}{\sigma_{2t}\sigma_{2c}}; \quad F_{66} = \frac{1}{{\tau_{12}}^2}; \quad F_{12} = f^*\sqrt{F_{11}F_{22}}$$

where $-1 \leq f^* \leq 1$ (the default value of f^* is zero).

An additional type of failure criteria is the separate mode criteria. The characteristic of these criteria is that they separate the matrix failure criterion from the fiber failure criterion. An example of such type is the **Hashin criterion** which considers four different failure modes: fiber tension, fiber compression, matrix tension, and matrix compression. Using this criterion damage initiation takes place when any of the following

conditions is satisfied.

$$\left(\frac{\sigma_1}{\sigma_{1t}}\right)^2 + \left(\frac{\sigma_6}{\tau_{12}}\right)^2 = 1 \quad \text{fiber tension } (\sigma_1 \geq 0) \tag{2.4.4}$$

$$\frac{\sigma_1}{\sigma_{1c}} = 1 \quad \text{fiber compression } (\sigma_1 < 0) \tag{2.4.5}$$

$$\left(\frac{\sigma_2}{\sigma_{2t}}\right)^2 + \left(\frac{\sigma_6}{\tau_{12}}\right)^2 = 1 \quad \text{matrix tension } (\sigma_2 \geq 0) \tag{2.4.6}$$

$$\left(\frac{\sigma_2}{2\tau_{23}}\right)^2 + \left[\left(\frac{\sigma_{2c}}{2\tau_{23}}\right)^2 - 1\right]\frac{\sigma_2}{\sigma_{2c}} + \left(\frac{\sigma_6}{\tau_{12}}\right)^2 = 1 \quad \text{matrix compression } (\sigma_2 < 0) \tag{2.4.7}$$

These conditions are valid prior to any damage initiation. Once damage initiation has occurred for at least one mode the stresses have to be substituted with so called effective stresses computed by introducing damage variables. For more information see [6].

2.5 Delamination

There are three basic fracture modes, illustrated in Figure 2.5.1. These failure modes are defined as opening mode (mode I), sliding shear mode (mode II) and tearing shear mode (mode III). Delaminations can be formed in each of these modes or as a combination of several modes, so called mixed mode delamination. The delamination process in a laminate occurs in two main steps: damage initiation and damage propagation. By performing standard tests experimental values associated with these steps can be evaluated for each fracture mode. These values need to be known when modeling delamination. This is explained in more detail in the next section 2.5.1

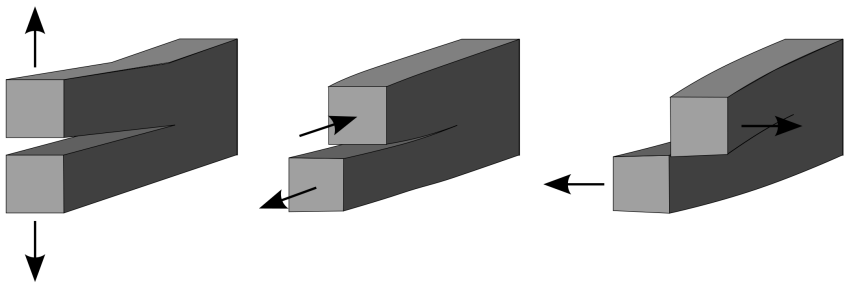

(a) *Mode I - opening.* (b) *Mode II - sliding.* (c) *Mode III - tearing.*

Figure 2.5.1: *The three fracture modes.*

2.5.1 Cohesive zone modeling

There exist different ways to model delamination. In this thesis the cohesive zone method is used. One advantage with the cohesive zone method is that it is possible to predict both the initiation and the propagation of the delamination. Moreover, it is not necessary knowing the location of the crack initiation and the direction of propagation in advance, cf. [7].

In the cohesive zone method interface elements are used together with a traction-separation law which relates the element tractions to the opening displacements, see Figure 2.5.2. As seen in the figure there is an initial elastic region until the peak traction, which is defined as the interlaminar strength, is reached. Thereafter follows a softening region until zero traction is reached. At this point element failure occurs which implies propagation of the delamination. The total area under the curve is equal to the critical energy release rate, often also defined as the fracture toughness of the material.

There exists several different damage initiation criteria. Throughout this thesis work the quadratic nominal stress criterion is used. If σ_3, τ_{13} and τ_{23} denotes the normal and the two shear tractions this criterion is

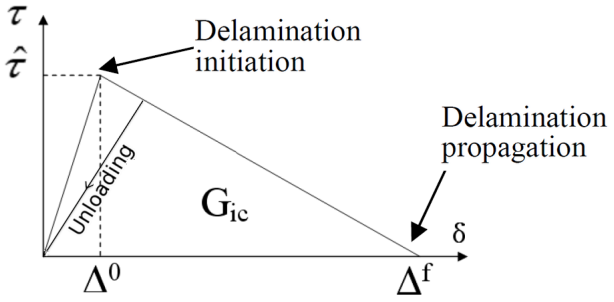

Figure 2.5.2: *Linear traction-separation response in cohesive elements (modified from [8]).*

defined as

$$\left(\frac{\langle\sigma_3\rangle}{\hat{\sigma}_3}\right)^2+\left(\frac{\tau_{13}}{\hat{\tau}_{13}}\right)^2+\left(\frac{\tau_{23}}{\hat{\tau}_{23}}\right)^2=1 \tag{2.5.1}$$

where $\hat{\sigma}_3$, $\hat{\tau}_{13}$ and $\hat{\tau}_{23}$ represent the peak values for delamination initiation when the deformation is either purely normal to the interface or purely in the first or the second shear direction, respectively. The symbol, $\langle\rangle$, represents the Macaulay brackets which signify that the compressive stress does not contribute to damage initiation [6].

Once the initiation criterion is reached, the material stiffness is degraded. The degree of stiffness softening is described by the damage variable D. Initially, when the interface is undamaged it has a value equal to zero and when the interface is fully damaged D is equal to one. The influence of the damage variable on the stress components of the traction-separation model is described by the following expressions, cf. [5]:

$$\sigma_3=\begin{cases}(1-D)\bar{\sigma}_3, & \bar{\sigma}_3\geq 0\\ \bar{\sigma}_3, & \text{otherwise}\end{cases} \tag{2.5.2}$$

$$\tau_{13}=(1-D)\bar{\tau}_{13} \tag{2.5.3}$$

$$\tau_{23}=(1-D)\bar{\tau}_{23}, \tag{2.5.4}$$

where $\bar{\sigma}_3$, $\bar{\tau}_{13}$ and $\bar{\tau}_{23}$ are the effective stress components predicted by the elastic traction-separation behavior for the current strains without damage.

Most likely, the cohesive layer is subjected to mixed mode loading, i.e. more than one mode contribute in the failure process. In Figure 2.5.3 it is shown how the mixed mode traction-separation response is obtained in the case of isotropic shear behavior.

To define when failure occurs either the effective displacement corresponding to complete failure,Δ_m^f, or the energy dissipated due to failure, G_C, need to be specified. In this thesis work the energy-based damage evolution has been used. The critical energy release rate, G_C, depends on the mode mix and can, for example, be specified by use of either the power law failure criterion or the Benzeggagh-Kenane (B-K) criterion.

The power law failure criterion is according to [6] defined as

$$\left(\frac{G_I}{G_{IC}}\right)^\alpha+\left(\frac{G_{II}}{G_{IIC}}\right)^\alpha+\left(\frac{G_{III}}{G_{IIIC}}\right)^\alpha=1 \tag{2.5.5}$$

where $\alpha\in(1.0-2.0)$ is a parameter derived from mixed mode tests and G_{IC}, G_{IIC} G_{IIIC} are critical energy release rates required to cause failure in pure mode I (opening), pure mode II (shear sliding) and pure mode III (shear tearing), respectively [7]. When this condition is fulfilled the critical mixed mode fracture energy is given by

$$G_C=G_I+G_{II}+G_{III}. \tag{2.5.6}$$

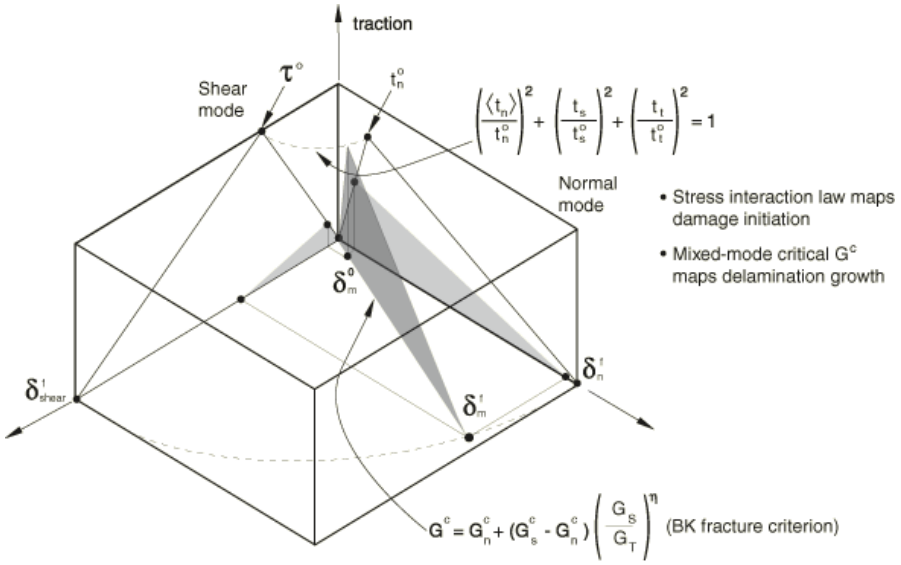

Figure 2.5.3: *Mixed mode response in cohesive elements (from [6]).*

Using the Benzeggagh-Kenane (B-K) criterion the critical mixed mode fracture energy is given by the following relation

$$G_{IC} + (G_{IIC} - G_{IC}) \left(\frac{G_{II} + G_{III}}{G_I + G_{II} + G_{III}} \right)^{\eta} = G_C \tag{2.5.7}$$

where η is a parameter determining the mixed mode ratio. Normally $\eta \in (1.0 - 2.0)$, cf. [6].

Finally, the last thing that needs to be specified is the softening part of the traction separation curve. This can either be defined as linear or exponential by the damage parameter D cf. [5] and [6]. In the analyses presented herein linear softening has been used.

2.5.2 Cohesive zone length

For the cohesive layer to properly capture delamination behavior the cohesive zone length must span a minimum number of elements, cf. [7]. The cohesive zone length is defined as the length ahead of the crack tip over which irreversible deformation occurs. Numerically this means the length over which the interface elements lies on the softening part of their traction-displacement response. At the end of the cohesive zone, the stress is equal to the interface strength. Analyses have shown that the cohesive zone needs to consist of 2-3 elements. Therefore, to ensure that there are enough interface elements, a sufficiently fine mesh is required. Another way to solve this problem is to artificially increase the cohesive zone length by decreasing the strength in the traction separation law.

2.6 Optimization

The general purpose of an optimization problem is to maximize, minimize or achieve a target value for a certain function, cf. [9]. This function is most often called the objective function and is denoted $f(x)$. The response functions of the optimization problem are normally restricted to certain limits that need no be satisfied to get an acceptable design. Those restricted response functions are called constraints, $g(x)$.

In the optimization study the Adaptive Response Surface Method (ARSM) is used. This method approximates the objective and constraint functions by a second order polynomial of the design variables x on the following form, cf. [9]

$$g_j(\mathbf{x}) \approx \hat{g}_j(\mathbf{x}) = a_{j0} + \sum_{i}^{n} a_{ji}x_i + \sum_{i}^{n}\sum_{k}^{n} a_{jik}x_i x_k \quad j = 1...m+1 \tag{2.6.1}$$

where m is the number of constraints, n is the number of design variables, and $a_{j0},\ a_{ji},\ a_{jik}$ are the polynomial coefficients which are determined by performing a least squares fit of the functions on to the previous design points. A more detailed description of the optimization procedure can be found in [9].

3 Method

This chapter describes the methods that have been used in the different parts of the work. It starts by describing the modeling of delamination benchmark tests. After that follows a section describing the material modeling. This is then used in the modeling of the four-point-bending test and of the orthosis which are presented in the following sections. At the end of the chapter the optimization method is described.

3.1 Delamination modeling

In order to investigate how to model the delamination and determine the optimal parameters for this kind of simulation, a couple of benchmark tests are studied. The fracture tests studied are the double cantilever beam (DCB) for mode I loading, the 3-point end notch flexure (3ENF) for mode II loading and the fixed ratio mixed mode (FRMM) for combined mode I and mode II loading. The set-up for the models can be seen in Figure 3.1.1.

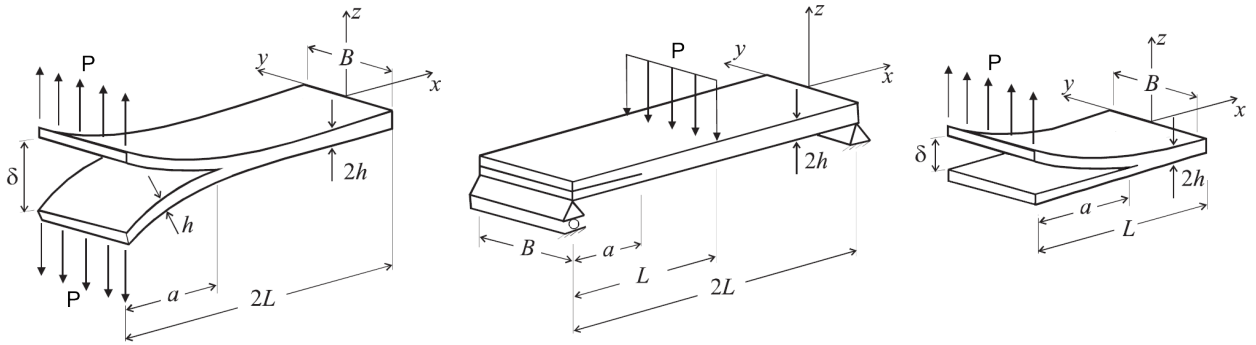

(a) *DCB* (b) *ENF* (c) *FRMM*

Figure 3.1.1: *Interlaminar fracture specimens (modified from [10]).*

The geometry parameters for the specimens and the material data for the test cases are specified in Table 3.1.1 and Table 3.1.2. The values are set as in [7] in order to be able to verify the obtained results.

Table 3.1.1: Geometry data for the test specimen.

L [mm]	50
B [mm]	20
$2h$ [mm]	35
a_0 [mm]	35

Table 3.1.2: Material properties for the test cases. (HTA6376/C)

(a) Composite properties.

E_1 [MPa]	120000
$E_2 = E_3$ [MPa]	10500
$G_{12} = G_{13}$ [MPa]	5250
G_{23} [MPa]	3480
$\nu_{12} = \nu_{13}$	0.3
ν_{23}	0.51

(b) Interface properties.

G_{IC} [N/m]	260
G_{IIC} [N/m]	1002
σ [MPa]	30
τ [MPa]	60

3.1.1 Set-up of the model

Models for the three benchmark tests were implemented in Abaqus/CAE. A various number of different approaches were tested. In this section the setup of the model is described.

To model the delamination the cohesive zone method was used. The theory behind this method is described in section 2.5.1. In Abaqus cohesive zones can be implemented in two different ways; by use of cohesive element or by using a cohesive contact formulation. The formulations used in the methods are very similar to each other. In this study they are both tested in order to investigate which one is best suited for the following models in the thesis work.

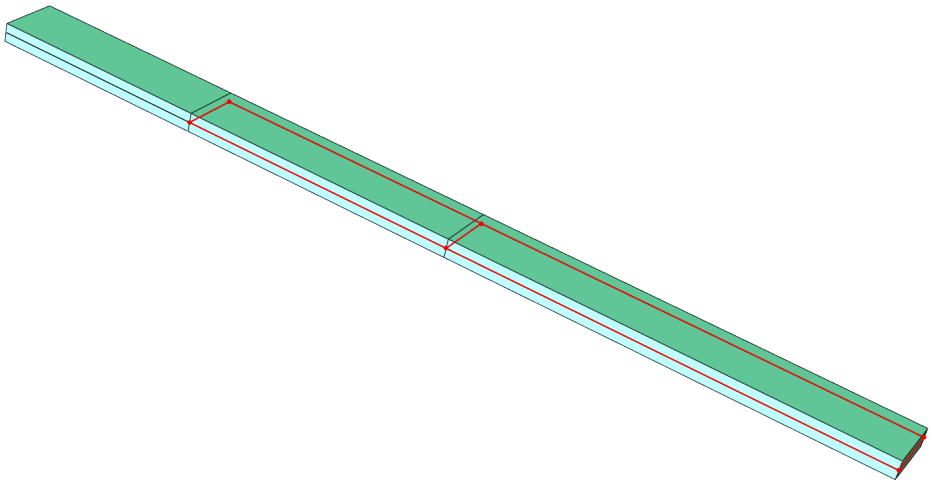

Figure 3.1.2: *Geometry of the delamination test specimen. Cohesive elements or cohesive contacts are inserted between the cantilevers in the red area.*

Cohesive elements (COH3D8) were added as a very thin element layer (thickness $10\mu m$) between the two cantilevers in the area shown in Figure 3.1.2. The mesh of the cohesive layer was matched to the mesh of the adjacent cantilevers. Hence, the cohesive elements could easily be connected to the elements on the other surfaces simply by sharing nodes. A close-up of the interface elements near the crack tip is shown in Figure 3.1.3. The constitutive response of the cohesive elements was defined using a traction-separation law. The material parameters for the cohesive zone were defined according to Table 3.1.2b. To compensate for the thickness of the cohesive layer the stiffness of the interface was specified as the material stiffness divided by the initial thickness of the cohesive layer. The damage was assumed to initiate when the quadratic stress criterion given in Equation 2.5.1 was satisfied. For the damage evolution the power law criterion, given by Equation 2.5.5, was used with α equal to one.

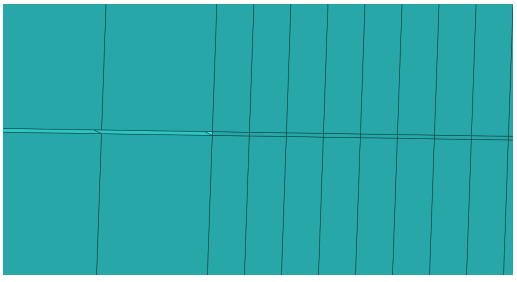

Figure 3.1.3: *Close-up of the interface elements near the crack tip*

When using the surface-based cohesive contact method the two cantilevers were set as different parts. The surface-based cohesive behavior was defined as a surface interaction property. This was done by defining the surface of one of the cantilevers as master surface and connect it to slave nodes of the other cantilever. Using this method no separation between the surfaces was necessary. The contact was inserted in the same area shown in Figure 3.1.2. The same interaction properties were used in this case as for the cohesive elements. To improve the convergence in both methods viscous regularization was used. More information about different

options for the cohesive interface can be found in [6].

The geometry and the mesh of the test specimen are shown together in Figure 3.1.4 . In the figure it can be seen that the mesh is denser close to the crack tip (the element length here is set to $0.1mm$). The reason for this is that a certain number of elements are required to span the cohesive zone in order to be able to model the delamination behavior in a correct way. In the study a couple of different element lengths were tested in order to check which length that was needed to achieve accurate results.

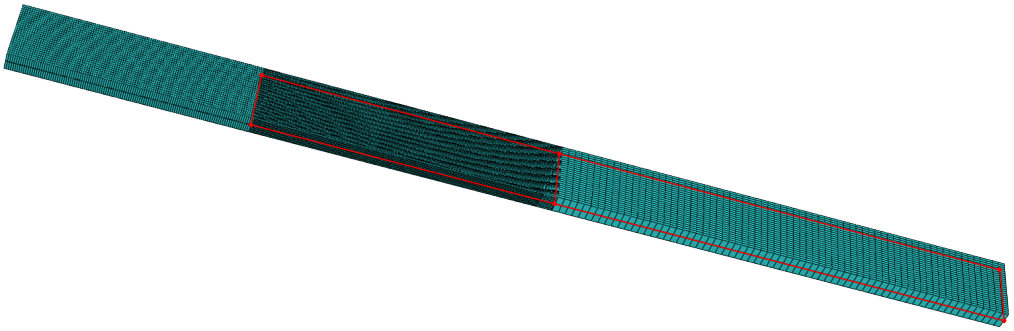

Figure 3.1.4: *Mesh of the delamination test specimen. The mesh is denser close to the crack in order to capture the delamination behavior of the cohesive elements.*

The loading of the test specimens, as shown in Figure 3.1.1, were applied by controlled displacement. For the DCB specimen the displacements were applied in opposite directions at the end edges of the crack side. For the ENF specimen a downward displacement was applied at the mid-span of the specimen. The displacement for the FRMM specimen was just applied on the end of the upper cantilever.

The other end was assumed to be completely fixed for both the DCB- and the FRMM specimen. The ENF specimen was modeled using simply supported boundary conditions.

To reduce the computing time, symmetry boundary conditions along the length was used to model just one half of the plate. For the ENF specimen a surface-to-surface contact was introduced between the two cantilevers (where there was no cohesive interface) in order to avoid that they will intersect each other.

Three different element types were tested in the simulations of the laminate: shell elements (S4R), continuum shells elements (SC8R), and solid elements (C3D8R). The R in the element denotation stands for reduced integration which means that fewer integration point are used in the calculations. Simpson's integration rule was used for all the elements.

3.2 The composite material

The composite material which is used in the orthosis is a pre-impregnated (short: pre-preg) material which consists of epoxy reinforced by carbon fibers. The carbon fibers are woven into a 4x4 twill as seen in Figure 3.2.1. For this material each line in the figure consists of approximately 3000 fibers. Woven fabrics are normally assigned a weft and a warp direction. Fibers running along the length are referred to as warp fibers, and those running across the width are defined as weft fibers. In this case, with a 4x4 twill and only one type of fibers, there is no difference between the weft and warp direction.

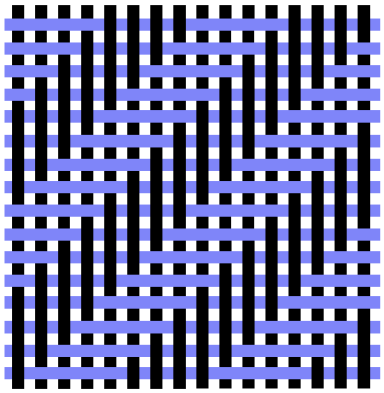

Figure 3.2.1: *Schematic of a 4x4 twill weave.*

The material is manufactured by Advanced Composite Group (ACG) and its properties are listed in Table 3.2.1. Since there is no difference between the weft and warp direction the material properties in the 2-direction are the same as in the 1-direction.

Table 3.2.1: Material properties for the composite (VTM266/CF0100).

Fiber volume fraction	v_f	0.5	-
Tensile modulus	E_{1t}	60.0	GPa
Tensile strength	σ_{1t}	700	MPa
Compressive modulus	E_{1c}	54.1	GPa
Compressive strength	σ_{1c}	541	MPa
Shear modulus	G_{12}	3.87	GPa
In-plane shear strength	τ_{12}	95.5	MPa
Inter-laminar shear strength	τ_{23}	71.4	MPa
Poisson's ratio	ν_{12}	0.3	-

When creating the orthosis, plies of the pre-impregnated material are cut out and pressed together. This procedure is done by hand of orthopedic technicians and may lead to large variations in the material properties in for example fiber angles and quality. Since the applied pressure is not constant the void fraction may also differ a lot from time to time. Applying pressure to the material causes a bit of the epoxy to pour out and consequently increase the fiber fraction, v_f. This implies that the material parameters provided by the manufactures are no longer valid for the final product. To adjust the material parameters micro-mechanics, as described in section 2.2, can be used.

3.3 Four-point bending test

To be able to verify the material model of the composite a simulation was made of a four point bending test of rectangular specimens made the same way as the orthosis. The test was conducted by SP Technical Research Institute of Sweden and the set-up can be seen in Figure 3.3.1. The two upper rollers were moved downward against the specimen at a constant velocity of 5 mm/min. The force applied by these rollers was measured together with the displacement until ultimate failure occurred. Nine different specimens were tested and the results are presented in Appendix B.

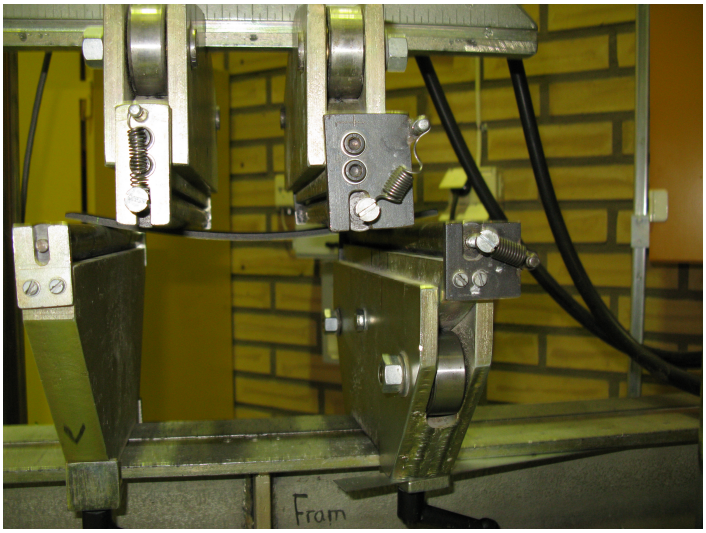

Figure 3.3.1: *Set-up of the 4-point bending test.*

The test specimen was made of 18 layers of the pre-preg twill, stacked [[0/90]/[±45]]. As can be seen in Table B.0.1 in Appendix B the thickness differed quite a lot among the test specimens. As described in the previous section this affects the material properties. Three different specimens were modeled with thickness set equal to the thickness of test specimens number 3, number 7 and number 9. Giving the thickness and the density for the epoxy and the the carbon fiber, the fiber volume fraction, v_f, for the specimens were calculated and the material properties subsequently defined using micro mechanics equations, see section 2.2.

The model of the four point bending test can be seen in Figure 3.3.2. To reduce the computing time, symmetry boundary conditions are often used to model just a half or a quarter of the specimen. In this case this is not possible since the composite laminate contains unsymmetrical plies stacked in the ±45° direction. The plate was modeled with continuum shells (SC8R) using both just one element layer and one element layer for each ply through the thickness.

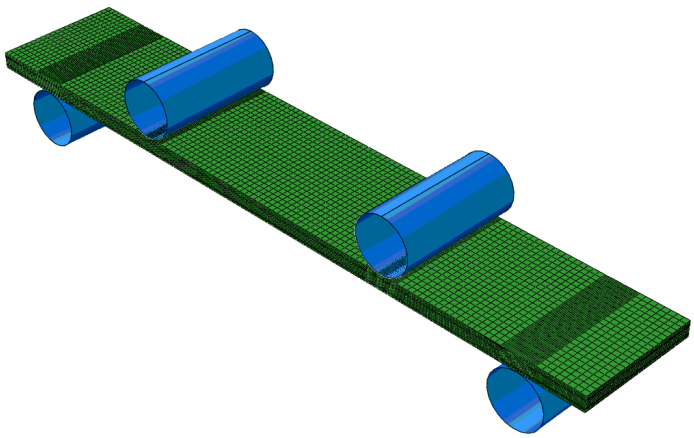

Figure 3.3.2: *Model of the 4-point bending test.*

The rolls were modeled as rigid bodies. Between the rolls and the plate a contact interaction was introduced. In this work the augmented Lagrange formulation was used and the friction was modeled using a penalty method with the friction coefficient set to 0.2. This was the settings which showed the best results in the previous thesis work. For more information see [2] and [6]. As seen in Figure 3.3.2 the mesh of the plate is refined around the contact points of the rolls in order to properly capture the contact behavior.

Failure criteria, such as the Hashin criterion described in section 2.4, were added to the model to capture failure of the fibers and matrix. In order to capture the delamination behavior which could be studied in the failed four point bending specimens cohesive layers were also added to the model. The cohesive layers were inserted in the middle and near the top and bottom of the laminate (more exactly after the second, 8th and 16th ply). The constitutive response of the cohesive elements was defined the same way as in the delamination modeling with the difference that the Benzeggagh-Kenane (B-K) criterion was used for the damage evolution. The same fracture toughness as in the delamination modeling, given in Table 3.1.2b, was used since no other data existed for the tested material.

3.4 Orthosis

In this section the FE-modeling of the orthosis is described. The section contains information about the mesh, the composite layup, the cohesive interaction and the boundary conditions.

3.4.1 Mesh

The geometry was meshed in the pre-processor Ansa using a cleaned up geometry of the scanned orthosis from the previous thesis work [2]. The inner surface of the orthosis was used for the geometry. The mesh consisted of approximately 2500 elements, the majority of them quadrilateral. The mesh is shown in Figure 3.4.1. A quite coarse mesh was chosen in order to keep the computing time for the optimization study on a reasonable level. The elements in the arch of the orthosis were adopted to follow the boundaries of the different plies.

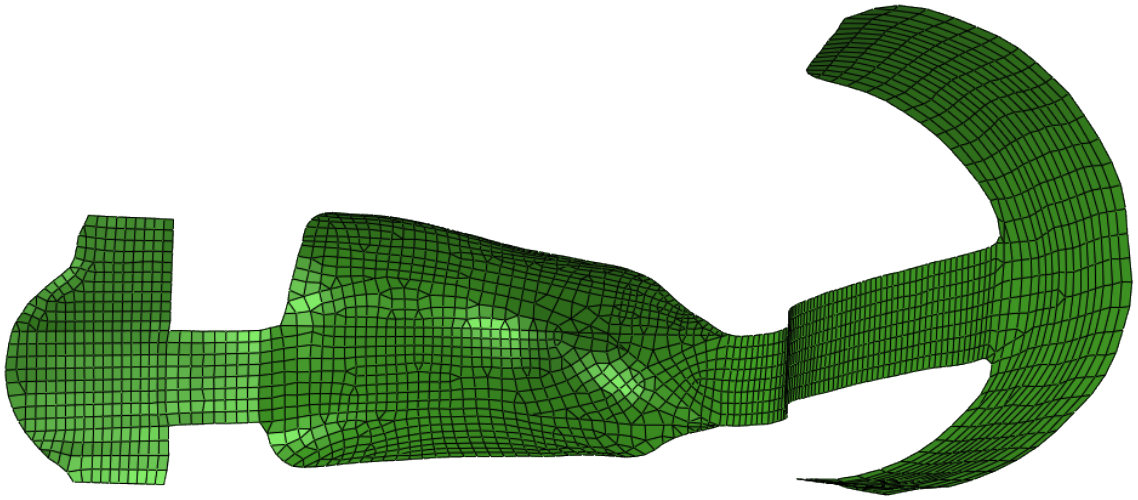

Figure 3.4.1: *The mesh of the orthosis.*

3.4.2 Composite layup

To create the composite layup Composites Modeler was used which is a kinematic draping tool developed by Simulayt Inc. Composites Modeler is used as a plug-in to Abaqus to improve the modeling of composite behaviors. By using Composites Modeler it is possible to simulate the draping of the different plies in a more realistic way. For example when a ply is draped to a curved area it becomes stretched and the original angle between the warp and weft directions changes. Composite Modeler takes this into account when modeling a laminate. Another advantage of Composite Modeler is that it is quite easy to specify the material orientations for the composite. The fiber directions can for example be specified to follow certain curves, so called seed curves.

There are several ways to model the composite layup. The layup used in this study was made starting from the meshed shell surface of the orthosis. The properties of the plies and the configuration of the layup were then specified and mapped onto the surface. Applying this method the draped lamina information was stored in different sections of the shell elements (S3R and S4R). When creating the shell properties the coordinate system that defines the material orientations need to be specified. Abaqus then automatically calculates the material orientation by transforming this coordinate system to each element. Since the orthosis is L-shaped the normal of the elements in the lower horizontal part are perpendicular to elements in the upper vertical part which caused some problem. To solve the problem two different coordinate systems were used; one in the lower horizontal part and one in the upper vertical part. The two coordinate systems are shown in Figure 3.4.2. The first coordinate system was used for all elements as long as the angle between the 1-direction and the normal of the element was greater than the so called switch angle. For this model a switch angle of 65° was found to achieve the best result for the material orientations. Observe that the material orientations referred to here are the directions before the draping procedure, which causes the directions to change, is performed.

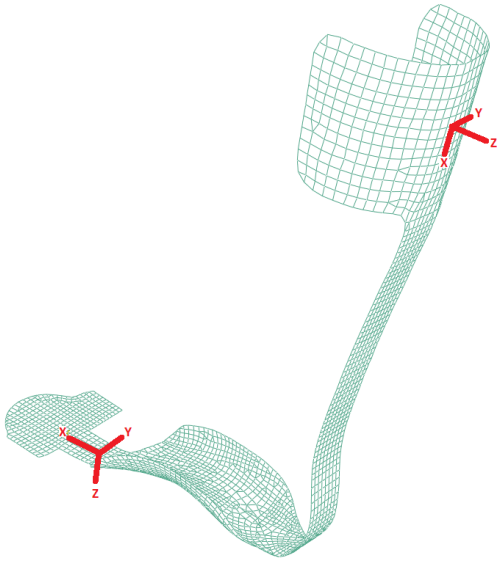

Figure 3.4.2: *The coordinate systems used to define the material orientations.*

3.4.3 Setup of the composite layup

In this study the same configuration of the layup of the orthosis has been used as in the previous thesis work, cf. [2]. This configuration is based on interviews of the engineers at the department of orthopedic technology at Borås Hospital, and observation of their work.

Ply regions, draping and ply stacking sequence

The analyzed orthosis is composed of 24 plies which are draped onto various regions. To make the layup, the orthosis is divided into different element sets corresponding to different ply regions. The top, the arch and the toe of the orthosis are each assigned an element set which can be seen in Figure 3.4.3. The spring is formed by four different element sets of approximately equal width taking different paths in the arch. Those sets are illustrated in Figure 3.4.4. For every ply a seed point to describe where the draping to start and a reference coordinate system need to be defined. More details about how to specify the different plies and make the composite layup can be found in [11].

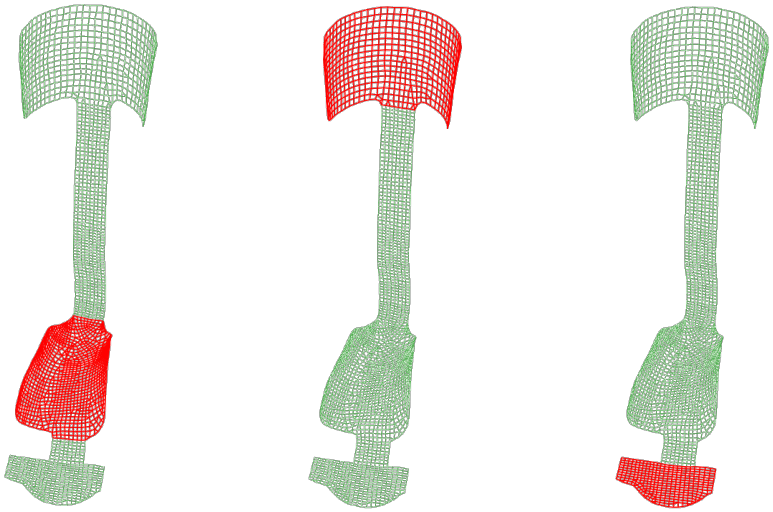

(a) *Arch element set.*

(b) *Top element set.*

(c) *Toe element set.*

Figure 3.4.3: *Element sets for the arch, toe and spring used in the draping simulation.*

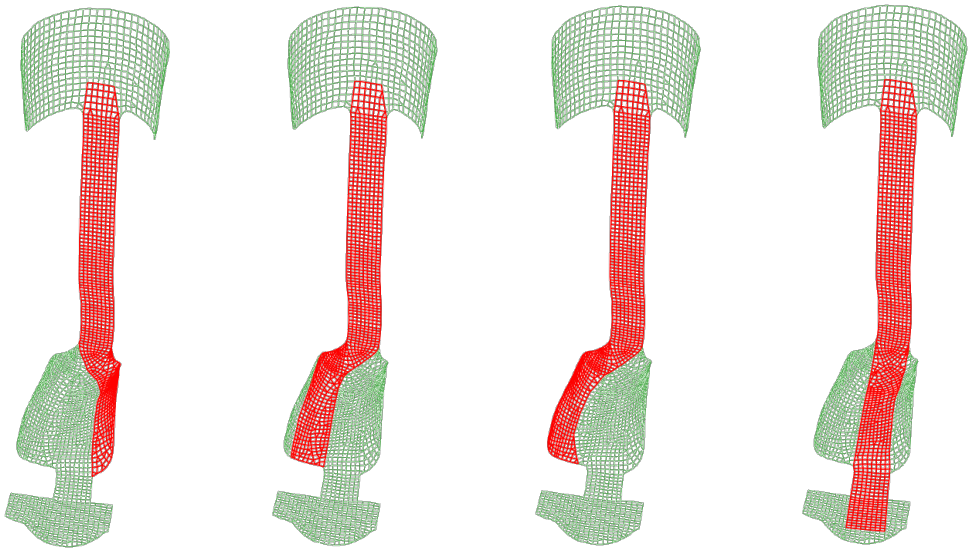

(a) *Left element set.* (b) *Right1 element set.* (c) *Right2 element set.* (d) *Straight element set.*

Figure 3.4.4: *The element sets forming the spring which are used in the draping simulation.*

These different plies are draped in the order defined in Table 3.4.1. In this table the original ply orientations can also be seen. The angles are set so that every other ply of the spring is orientated 45°. The draping order including the ply orientations of the laminate is often denoted as the ply stacking sequence. The layup with the ply stacking sequence described in Table 3.4.1 is in the continuation referred to as the original layup.

Table 3.4.1: The ply stacking sequence of the original layup for the orthosis, cf. [2] . Ply 1 is located closest to the foot.

Ply #	**Element set**	**Orientation**
1	Arch	45°
2	Top	0
3	Toe	0
4	Left	45°
5	Straight	0
6	Right1	45°
7	Straight	0
8	Right2	45°
9	Straight	0
10	Left	45°
11	Straight	0
12	Right1	45°
13	Straight	0
14	Right2	45°
15	Left	0
16	Right1	45°
17	Right2	0
18	Left	45°
19	Right1	0
20	Right2	45°
21	Left	0
22	Toe	0
23	Top	0
24	Arch	45°

Seed curves

To make the fiber direction correctly orientated in the plies seed curves are used. The seed curves constrain the warp or weft directions of the material along a path defined by element edges, cf. [11]. In the model the seed curves need to be used in the non-straight sets for the spring. The used seed curves are shown in Figure 3.4.5.

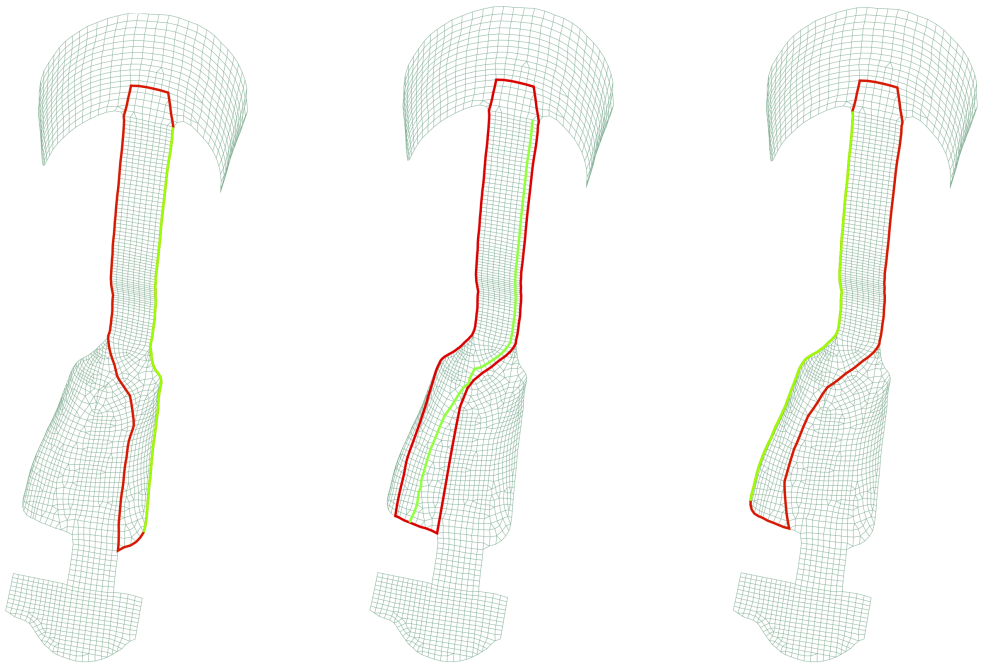

(a) *Left set.* (b) *Right1 set.* (c) *Right2 set.*

Figure 3.4.5: *The seed curves (lightgreen line) used in the non-straight sets for the spring.*

In Figure 3.4.6 the effect of using seed curve is shown for the ply given by the *left* element set. It can clearly be seen that the seed curve forces the fiber directions to follow the edge of the orthosis.

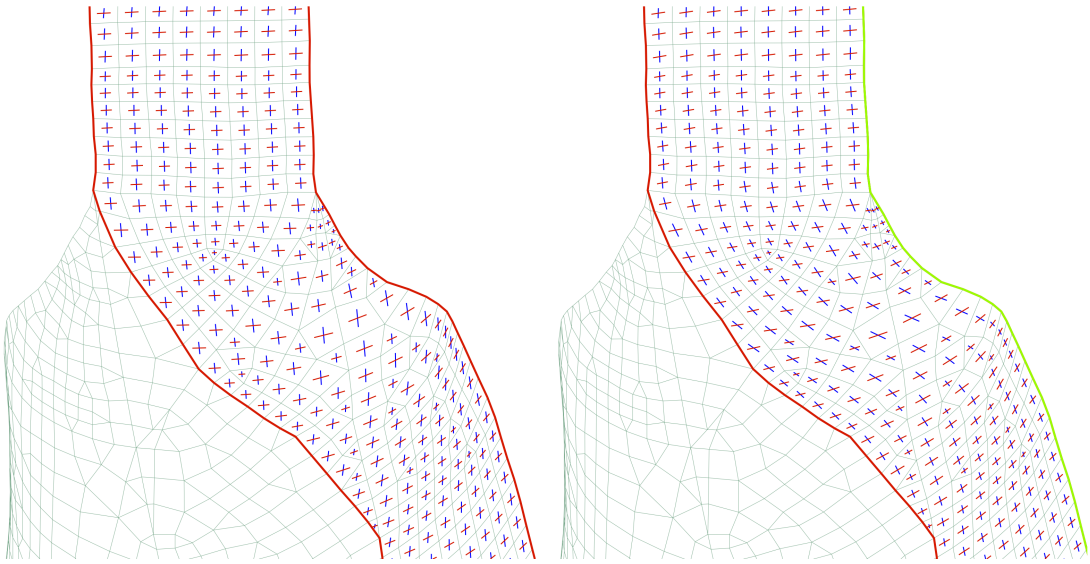

(a) *Without using seed curve.* (b) *Using seed curve.*

Figure 3.4.6: *Ply fiber directions without using and using seed curve. Warp directions are shown in blue and weft direction in red.*

The effect of using seed curves can also be illustrated as in Figure 3.4.7 where the ply draped patterns are shown for the two cases. Without using seed curve the warp and weft direction remains more or less perpendicular to each other. This is not the case if seed curves are used.

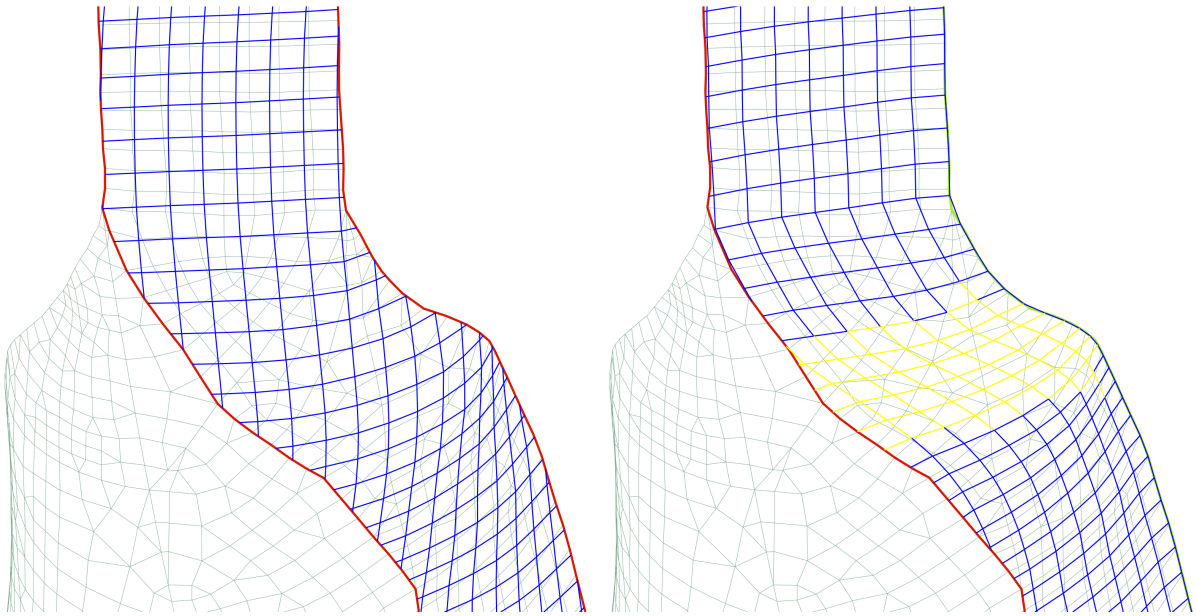

(a) *Without using seed curve.* (b) *Using seed curve.*

Figure 3.4.7: *Ply draped pattern without using and using seed curves. The yellow zone indicates that the warp and weft directions are no longer perpendicular.*

3.4.4 Cohesive zone

To be able to model delamination in the orthosis cohesive contacts were added to the model. Adding cohesive contacts leads to a significant increase in the computing time. Since it was important to keep the computing time short to be able to perform an optimization study, the cohesive contact was just added between the two middle layers (i.e. ply 12 and 13). The reason why the contact was inserted between those layers is that it is the most likely place for delamination to occur since it is where the shear stresses are highest in bending.

To be able to add the cohesive contact to the model, the orthosis needed to be divided into two parts, one containing ply 1-12 and one containing ply 13-24. The second part was made using an offset value to make the upper surface of ply 13 to be just in contact with the lower surface of ply 12. The same interface properties were used as in the modeling of the benchmark tests, these values are found in Table 3.1.2b.

Adding cohesive contacts between all elements resulted in delamination initiation in small edge elements in the arch which are not of interest. Hence, the cohesive contact was just added between the elements indicated in Figure 3.4.8. This area includes the area were the delaminations are observed to occur. The remaining elements were constrained by a tie contact between the two parts.

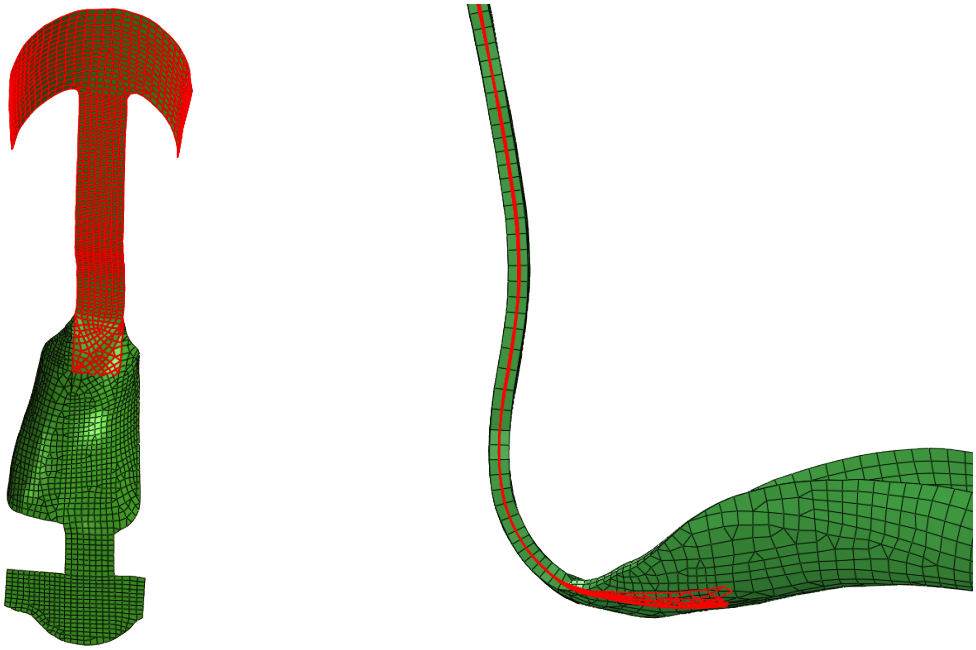

Figure 3.4.8: *The elements where the cohesive contact is applied are indicated by the red zone. The rest of the elements are constrained by a tie contact between the two parts.*

3.4.5 Boundary conditions

A load was applied to the orthosis by coupling the displacement of a set of nodes in the top of the spring. The displacement was set to reach a maximum of 15 *cm*. To achieve bending in the heel area a set of nodes in the arch was fixed. The boundary conditions are illustrated in Figure 3.4.9.

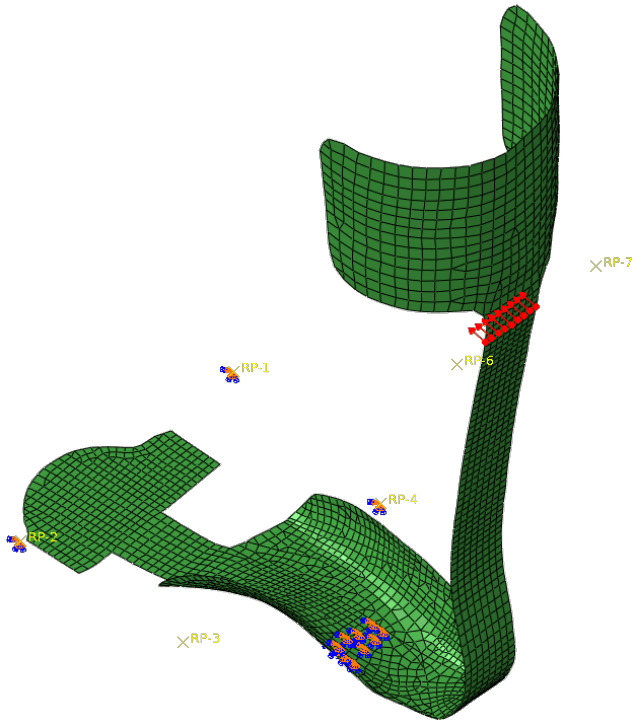

Figure 3.4.9: *The boundary conditions used for the orthosis.*

3.5 Ply orientation optimization

In order to improve the delamination performance of the orthosis an optimization study was performed. The objective with this study was to maximize the load before delamination begin to initiate in the orthosis. The design variables, i.e. the variables which are changed in the optimization, are the orientation of the 18 plies forming the spring. The design variables are each set to take any of the discrete values of 0° or 45°. As a constraint the stiffness of the spring needs to be kept more or less constant. The reason for this was that the orthopedic engineers did not wanted to affect the walking behavior of the orthosis. This is ensured by checking that the ratio between the reaction force and the corresponding displacement does not differ more than 5% from the values of the original layup given in Table 3.4.1. This ratio is checked in the beginning of the analysis, i.e for small displacements, meanwhile it still has a linear behavior. As an additional constraint the maximum Tsai-Wu value in the heel area shown in Figure 3.5.1a is not allowed to exceed the value of the original layup. For the optimization the Adaptive Response Surface Method (ARSM) was used (see section 2.6).

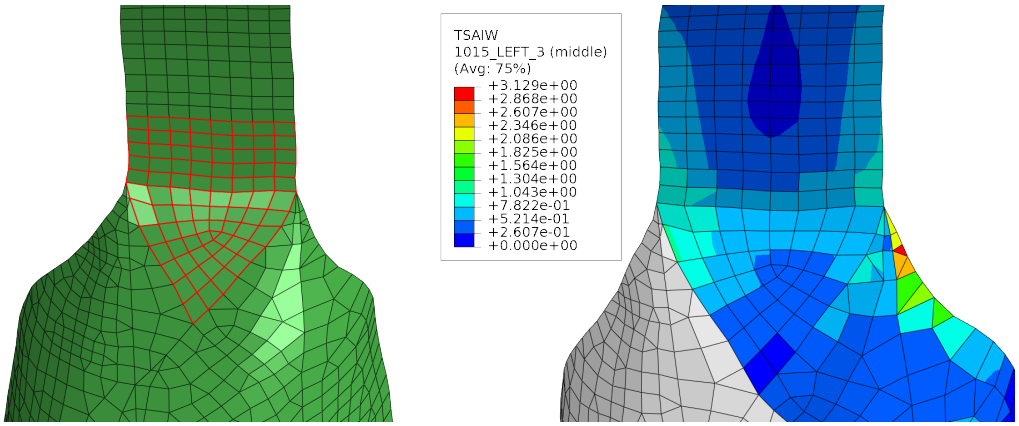

(a) *The zone in which the Tsai-Wu valus are checked.*

(b) *Maximum Tsai-Wu in the whole model.*

Figure 3.5.1: *The Tsai-wu values are checked in the highlighted area in the figure to the left to avoid the high values in the narrow elements forming the non-straight plies, which is seen to the right.*

The optimization was done using HyperStudy. In Figure 3.5.2 a schematic illustration of the optimization procedure is shown. In HyperStudy a python script is called which interacts with Abaqus. First, the script opens Composites Modeler and changes the fiber directions of the plies of interest. Draping of this new layup is also performed by Composites Modeler. The script then starts to run of the analysis and when it is done it prints the reaction force and corresponding displacement of the nodes (where the load is applied) to a text-file. The script also searches through all the composite layers of the orthosis in the heel area in order to find the maximum Tsai-Wu value. This value is also printed to a text-file which is read in HyperStudy.

It should be observed that it is the maximum load when the delamination begins to initiate and not when it begins to propagate which is studied in this optimization. The reason why this method is chosen is that the analysis encounters convergence problem and terminates when the initiation strength is reached. It should also be noted that this optimization study is a relative investigation. This means that the loads acquired for delamination initiation not necessarily coincide with reality. One cause for this is that the interface properties are not specified specifically for the composite in the orthosis. Even if the interface properties were chosen correctly the correct load for delamination initiation would probably not be obtained since the cohesive element length is quite large. To achieve correct values a finer mesh is needed or the strength for the traction-separation law needs to be adjusted to artificially increase the cohesive zone length. Since the optimization study just served to investigate a relative trend for reaching a better delamination initiation performance, the model was not refined further.

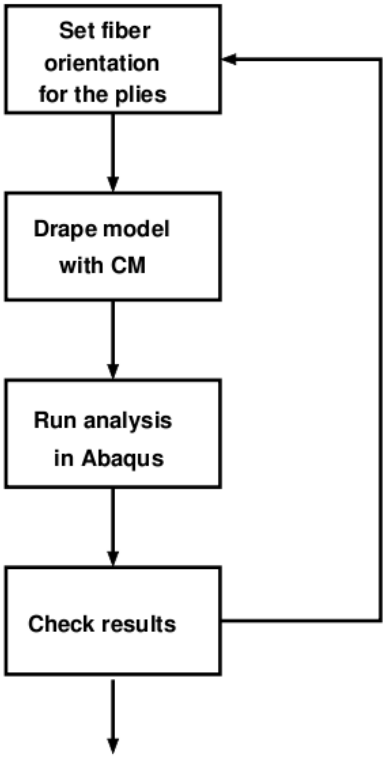

Figure 3.5.2: *The optimization procedure.*

.

4 Results

This chapter covers the results from the modeling of the delamination benchmark tests, the four point bending test and the orthosis calculations.

4.1 Delamination modeling

In this section the results from the modeling of the delamination benchmark test are presented. The deformations are shown for all the test cases and the corresponding force - displacement relation is plotted together with analytical curves obtained using the corrected beam theory presented in Appendix A. For the pure mode I and mode II tests there also exist experimental results presented in [7]. These experimental values correlate very well with the numerical ones.

4.1.1 Mode I DCB test

The deformation of the DCB specimen can be seen in Figure 4.1.1. In the figure the failed cohesive interface elements can be seen. Behind the failed elements a new crack tip has been formed.

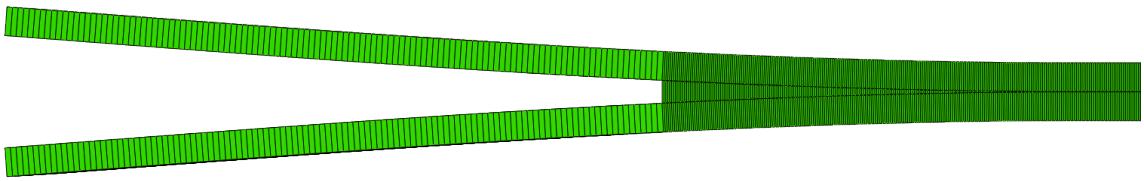

Figure 4.1.1: *Deformations in the DCB specimen.*

The propagation of the crack front can be studied by plotting the transversal stress in the cohesive layer as in Figure 4.1.2. In the figure, the location of the highest stress indicates the delamination initiation. Observe that it is only half of the width of the specimen that is modeled. This implies that the crack front, just as expected, travels faster in the center. As described in section 3.1.1 the delamination modeling was performed

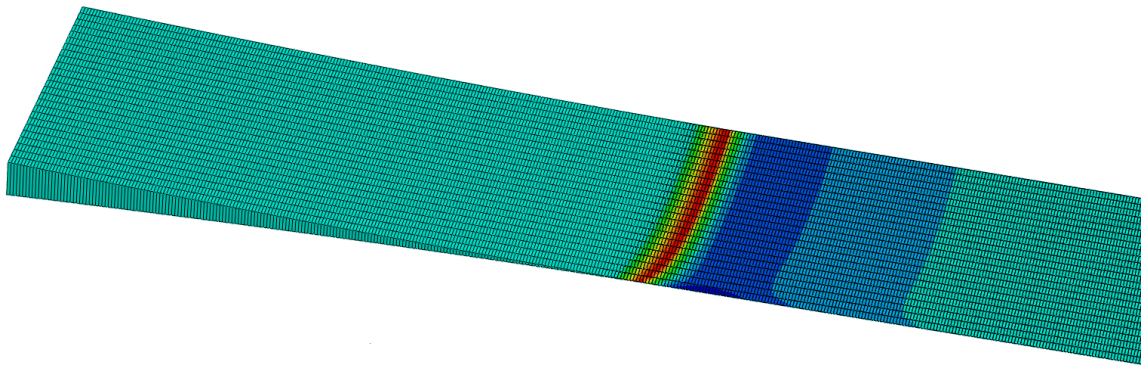

Figure 4.1.2: *Transversal stress in the cohesive layer. The red area indicates where the highest stress occur and consequently the curvature of the crack front.*

by testing different element types. Solid elements turned out to cause a lot of problems e.g. hourglassing effects [see [6]] as well as very long computing times whereafter this method was abandoned. Both using ordinary shell elements and continuum shell elements worked well and the results were exactly the same. The models were tested using both cohesive element and a cohesive contact formulation. Even in this case both methods

worked fine and neither could any difference in the result be found. In Figure 4.1.3 the force - displacement relation is shown for the different methods. Since all methods gave the same results the curves are difficult to distinguish. The remaining results in this section are obtained for continuum shells using cohesive elements.

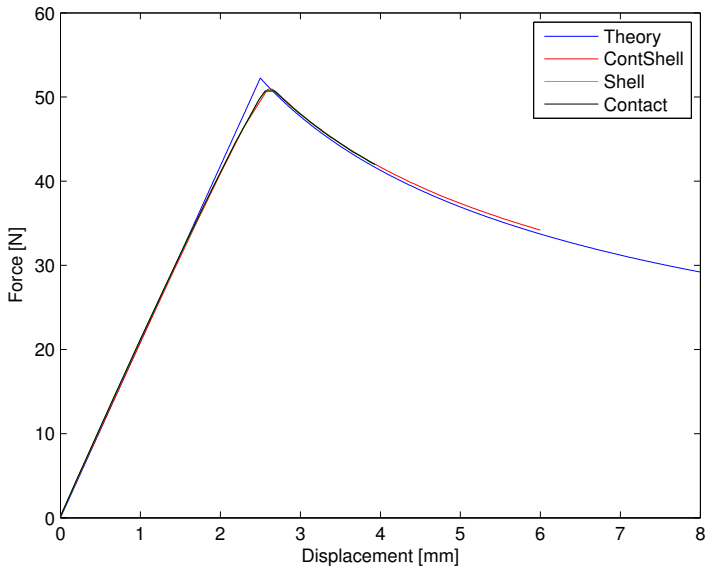

Figure 4.1.3: *Force - displacement relation for the DCB specimen.*

4.1.2 Mode II 3ENF test

In Figure 4.1.4 the deformation of the 3ENF specimen in the mode II test is shown. In this case the load causes a lateral movement between the cantilevers and the cohesive elements undergo shear deformation.

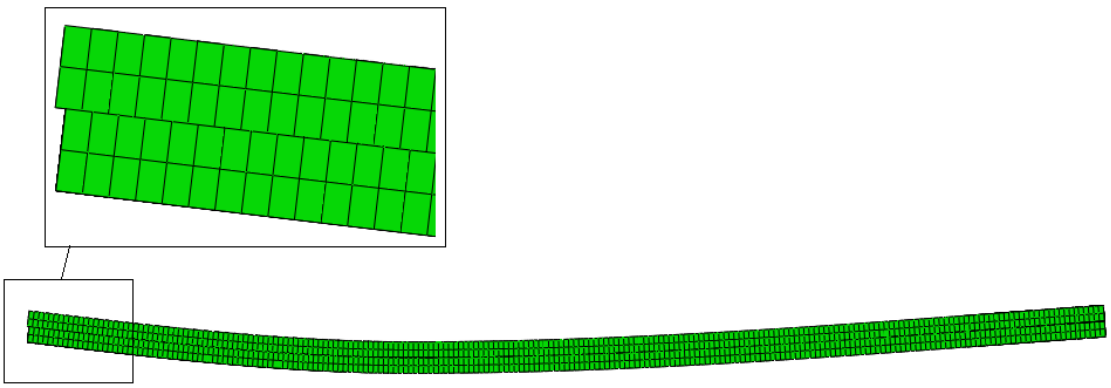

Figure 4.1.4: *Deformations in the 3ENF specimen.*

The force - displacement relation for this case is shown in Figure 4.1.5. As illustrated in the figure, there is a good correlation between the FE-model and beam theory.

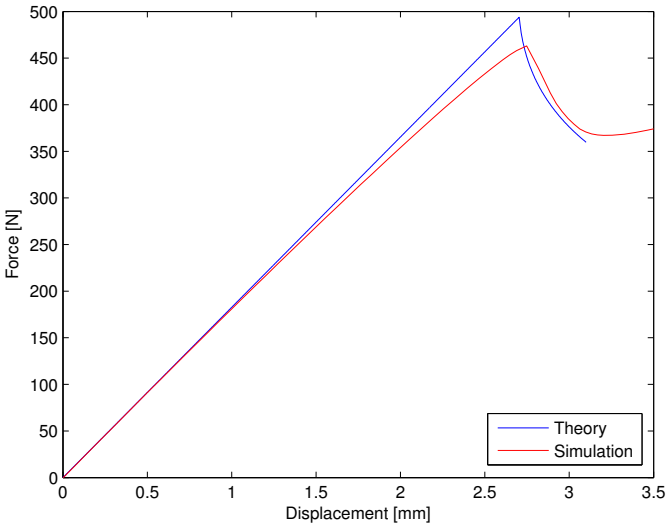

Figure 4.1.5: *Force - displacement relation for the 3ENF specimen.*

4.1.3 Mixed-mode (FRMM) test

For the case of mixed mode loading the cohesive elements experience both mode I and mode II deformation. This can can be observed in Figure 4.1.6.

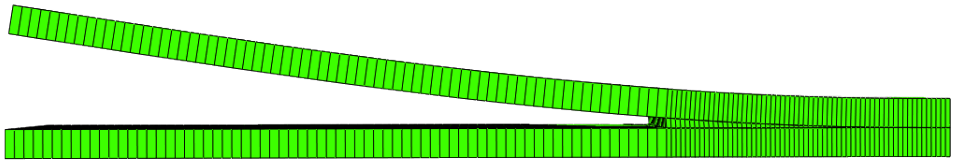

Figure 4.1.6: *Deformations in the FRMM specimen.*

In Figure 4.1.7 the force - displacement relation is shown for this case. As can be seen, the simulated values do not agree as well with the theoretical values as in the previous cases, but may still be considered good.

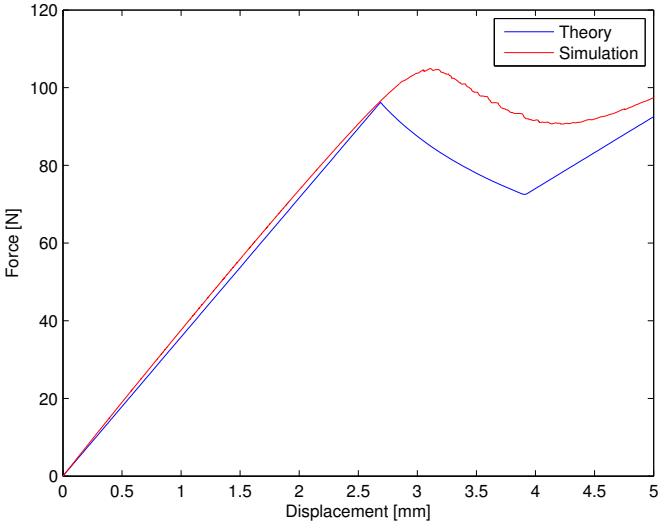

Figure 4.1.7: *Force - displacement relation for the FRMM specimen.*

4.2 Four-point bending test

In this section the results from the modeling of the four-point bending test are presented.The results are presented as force - displacement relations that are obtained by using different modeling methods for the tested specimens. In Figure 4.2.1 the force-displacement curves are presented for specimen number 9. In the figure it can be seen that the model using the Hashin failure criteria gives an accurate prediction of the load causing ultimate failure when the specimen is modeled with one element through the thickness. The corresponding displacement is however a bit lower than in the experiment. The deformation after ultimate failure for this model can be seen in Figure 4.2.2. Still using the Hashin damage criteria and modeling the specimen with one element layer per ply some dips in the force - displacement were captured. Those dips can also be observed in the experimental curves and are probably due to compression failure of the top ply under the rolls. Unfortunately the analysis experienced convergence problems after the load drop. These results are from the models without using cohesive layers. It was also tested to add cohesive layers in the model to capture the delamination behavior. When adding cohesive layers to the model with Hashin damage no difference in the results could be observed. It was also tested to use just cohesive layers without any other damage criteria and this result is also presented in Figure 4.2.1. It was found that the stresses in this case were too low for delamination initiation to occur. This is illustrated in Figure 4.2.3 where the factor of the quadratic nominal delamination initiation criteria is plotted. The delamination initiate when this factor equals one.

In all of the experimental curves there are some nonlinearities in the initiation of the test. It is hard to say what causes this deviation, one possible cause is friction. Omitting this initial deviation would improve the agreement between the experimental and modeled curves.

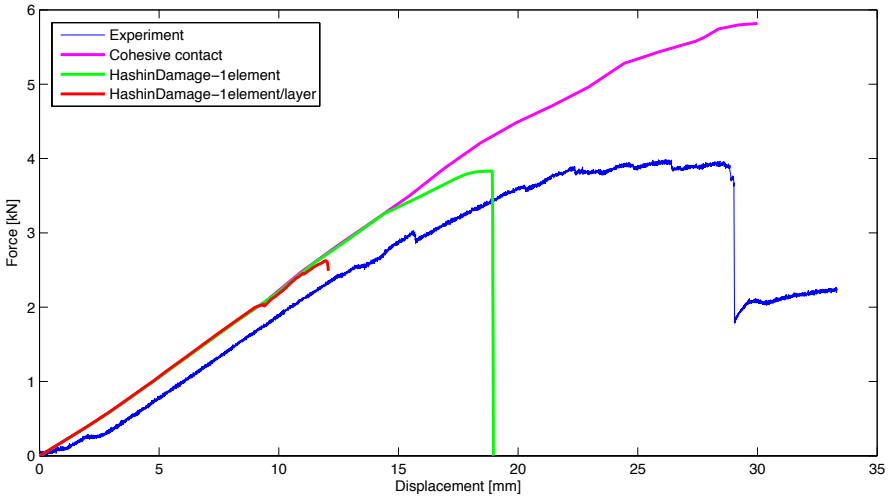

Figure 4.2.1: *Force - displacement relation for specimen no. 9 in the 4PB test.*

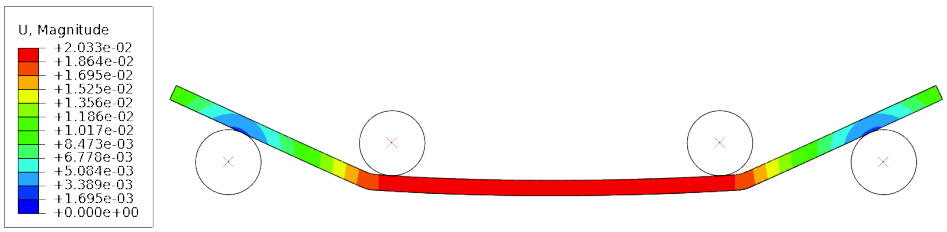

Figure 4.2.2: *Displacement (in [m]) after ultimate failure in the 4PB model using one element through the thickness and a Hashin damage model.*

The same force - displacement curves as presented above are also compared with the experimental curve for specimen number 7 since this specimen had exactly the same dimensions as specimen 9. The result is presented in Figure 4.2.4.

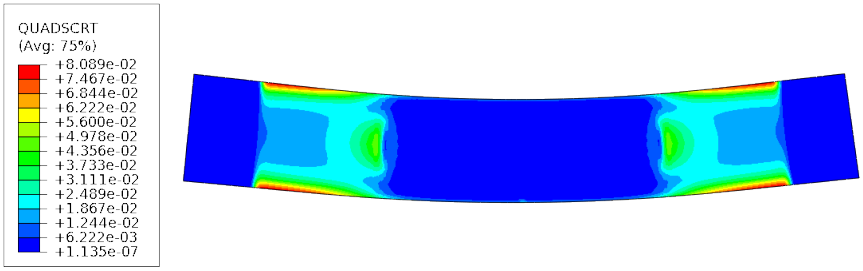

Figure 4.2.3: *Quadratic nominal stress delamination initiation criterion (see Equation 2.5.1.). The delamination initiate when this factor equals one.*

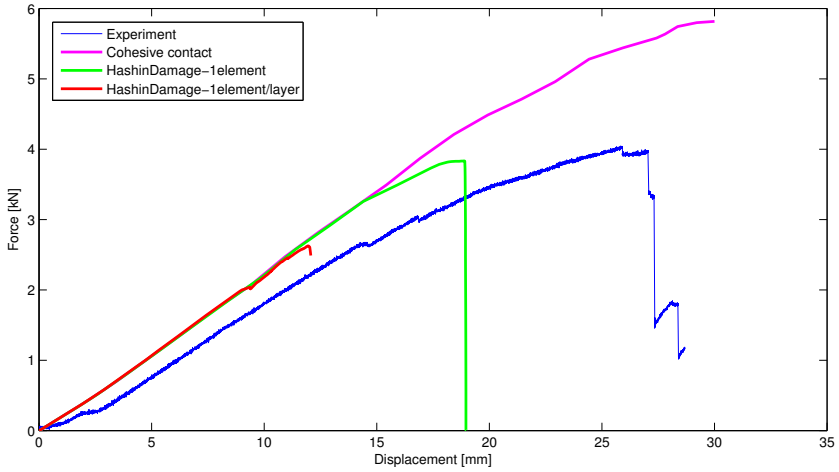

Figure 4.2.4: *Force - displacement relation for specimen 7 in the 4PB test.*

The modeling using the Hashin damage was also repeated for specimen number 3 and the results are presented in Figure 4.2.5. Even in this case the model with one element through the thickness gave the best estimation of the ultimate failure load while the model with one element layer per ply captured the assumed compressive failure of the top ply.

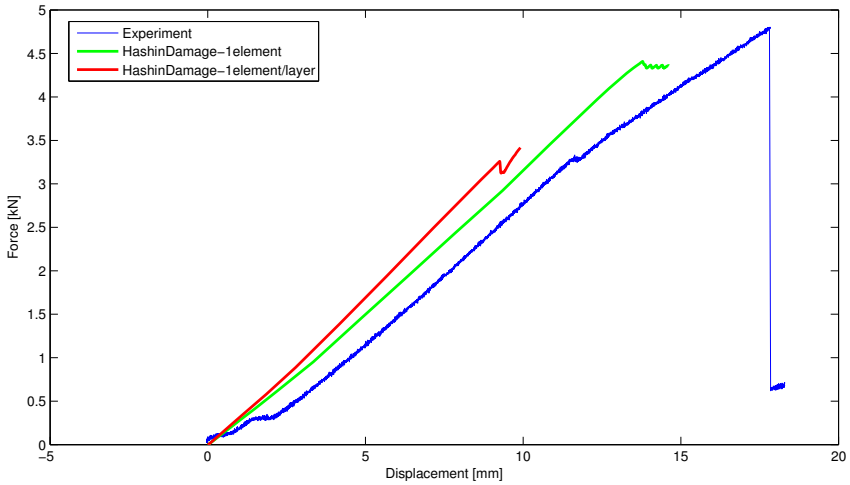

Figure 4.2.5: *Force - displacement relation for specimen 3 in the 4PB test.*

4.3 Orthosis

In this section the results from the modeling of the orthosis and the optimization are presented. As described in chapter 3.5 the optimization of the ply layup, with respect to the fiber angles, was performed by studying the load or rather the displacement that it was possible to apply before delamination began to initiate. In Figure 4.3.1 the deformation of the orthosis when delamination initiation occur is shown.

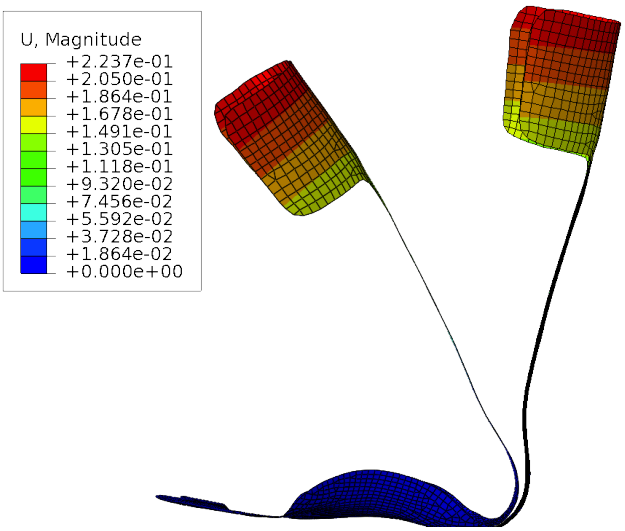

Figure 4.3.1: *The deformation (in [m]) of the orthosis causing delamination initiation. The deformation corresponds to an applied load of* $\sim 350\,N$ *at the top of the spring.*

The delamination is set to initiate when the quadratic nominal stress initiation criterion, given in Equation 2.5.1, is fulfilled. In Figure 4.3.2 the criterion is plotted for the original layup given in Table 3.4.1. In the figure delamination initiation is seen to occur in the center of the heel area where this variable equals one.

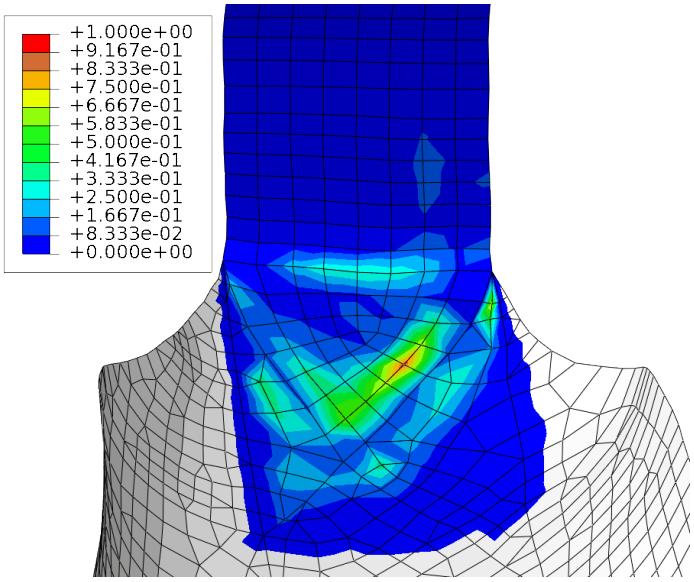

Figure 4.3.2: *Delamination initiation of the cohesive contact according to the quadratic nominal stress delamination initiation criterion (see Equation 2.5.1). In the center of the heel this factor equals one which means that delamination has been initiated.*

In addition to the stiffness constraint, the Tsai-Wu criterion described in section 2.4 was used. The maximum Tsai-Wu value of all of the layers in the heel area was set to not exceed the maximum value in the original layup which is shown in Figure 4.3.3.

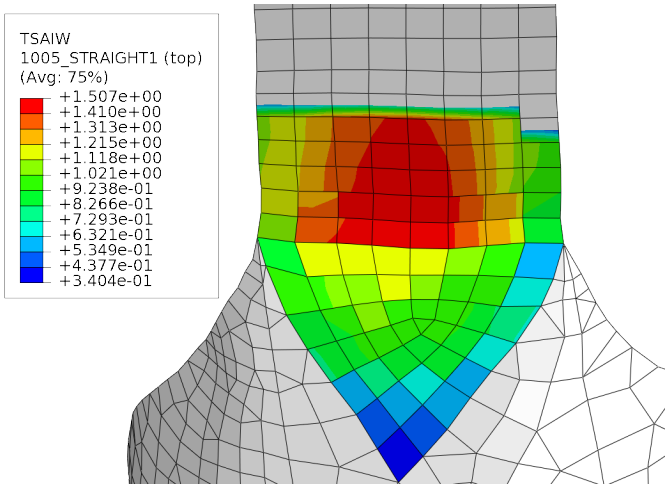

Figure 4.3.3: *The highest Tsai-Wu value (see Equation 2.4.3).*

The result from the optimization is shown in Figure 4.3.4. In the figure the applied displacement when delamination initiation occurs (i.e. the optimization objective) as a function of the iteration number for the optimization is plotted. The optimization procedure proceed from the original lay-up and in the subsequent eighteen iteration it sequentially change the orientation of one ply meanwhile the other orientations are unchanged.The optimization converges in iteration number 22 and the layup which can sustain the largest deformation and satisfies the constraint conditions is hence found. The ply stack angles for this lay-up are presented in Table 4.3.1. A more detailed table describing each iteration step is found in Appendix C.

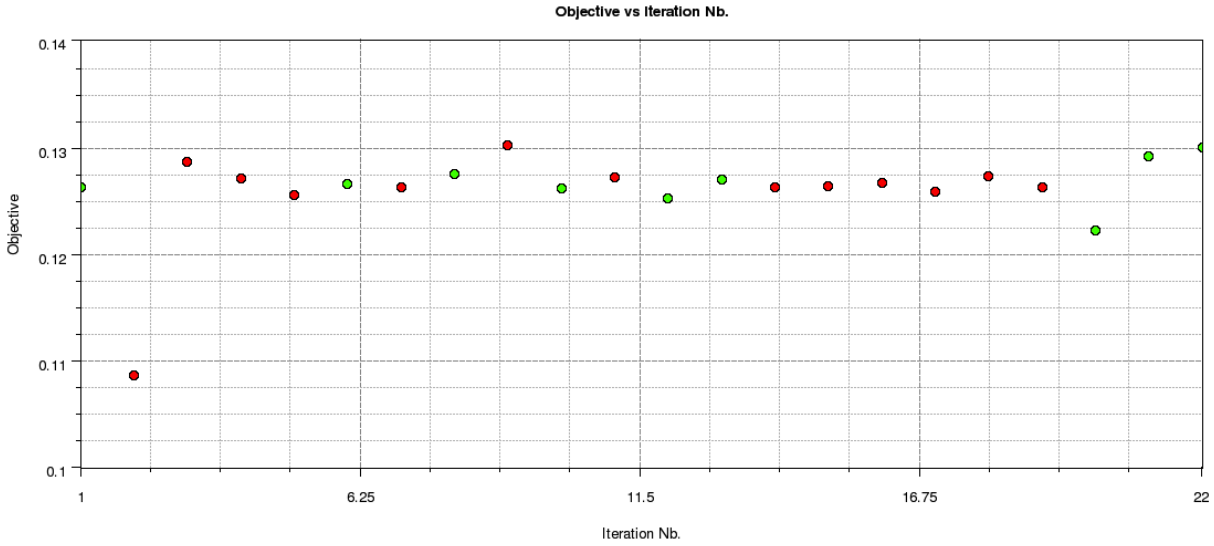

Figure 4.3.4: *The applied displacement (in [m]) when delamination initiation occur (i.e. the optimization objective) as a function of the iteration number for the optimization starting from the original ply layup. The green circles means that the constraint conditions are satisfied.*

In Figure 4.3.5 and Figure 4.3.6 the constraints are plotted as a function of the iteration number. Figure 4.3.5 shows the stiffness of the spring of the orthosis. The stiffness should lie in the interval indicated by the two red lines in the figure. This interval corresponds to a 5% divergence from the stiffness of the original layup. In the figure it can be seen that the stiffness of the orthosis only vary with the orientation of the outermost plies. The orientation of the six innermost plies, which are changed in iteration number 8 to number 13, have negligible effect on the stiffness. In Figure 4.3.6 the constraint which limits the Tsai-Wu value is shown.

Table 4.3.1: Results from the optimization starting from the original ply layup.

Layup	Fiber angle for ply #																		Stiff.	Tsai-Wu	Disp.
	01	02	03	04	05	06	07	08	09	10	11	12	13	14	15	16	17	18	$[N/m]$	-	$[m]$
Original	45	0	45	0	45	0	45	0	45	0	45	0	45	0	45	0	45	0	2885	1.512	0.1262
Optimal	45	45	0	0	45	0	45	45	45	0	45	0	45	0	45	0	45	0	2778	1.447	0.1299

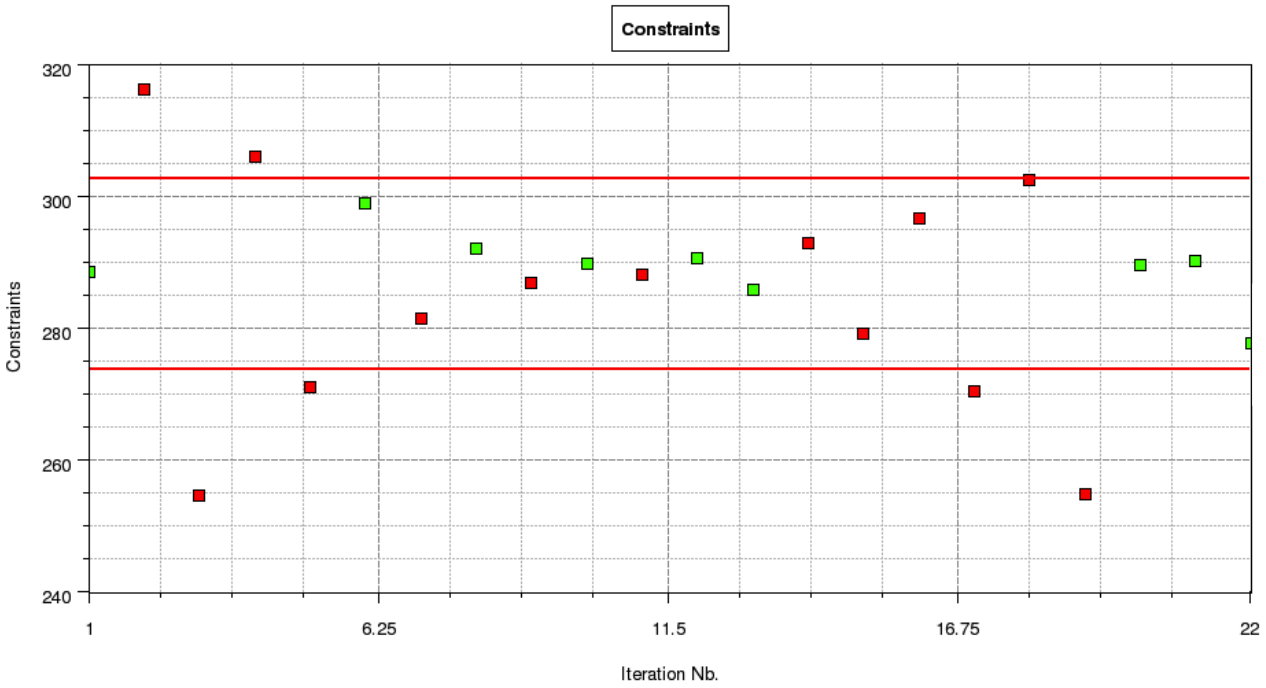

Figure 4.3.5: *The stiffness as function of the iteration number for the optimization starting from the original ply layup. The two red lines represents the upper and lower boundary for this constraint corresponding to a 5% divergence from the stiffness of the original layup.*

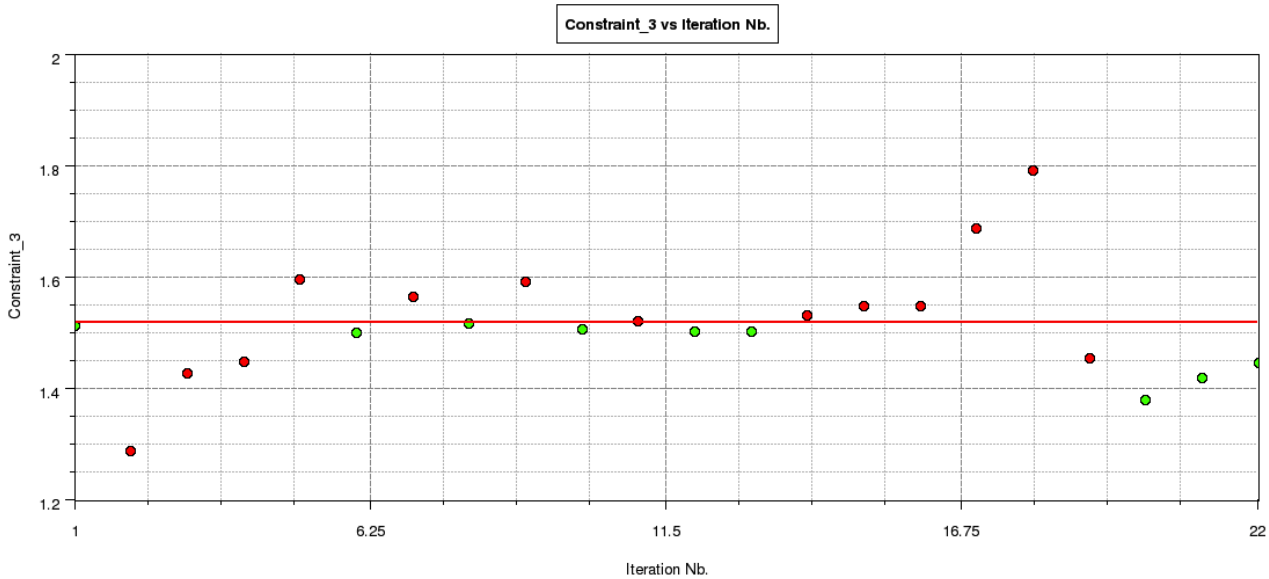

Figure 4.3.6: *The Tsai-Wu value as function of the iteration number for the optimization starting from the original ply layup. The red line represents the value of the original layup which must not be exceeded.*

The same optimization procedure was also performed starting from a layup with all plies oriented in the [0/90] direction instead of the original layup. The result is shown in Figure 4.3.7. As seen in the figure the best design was found in iteration number 22. However, the result for the displacement in this case is lower than for the original layup . In the figure it can also be noted that it was not until the final two iterations that the constraints were fulfilled. The constraints for the stiffness and the Tsai-Wu value are shown in Figure 4.3.8 and Figure 4.3.9. The ply stack angles for the found optimal layup in this case are shown in Table 4.3.2. More details about each iteration step can be found in Table C.0.2 in Appendix C. It was also tested to see which optimal layup that was obtained without constraining the Tsai-Wu values and the results are presented in Table C.0.3. Neither in this case was the found optimal result better than for the original layup.

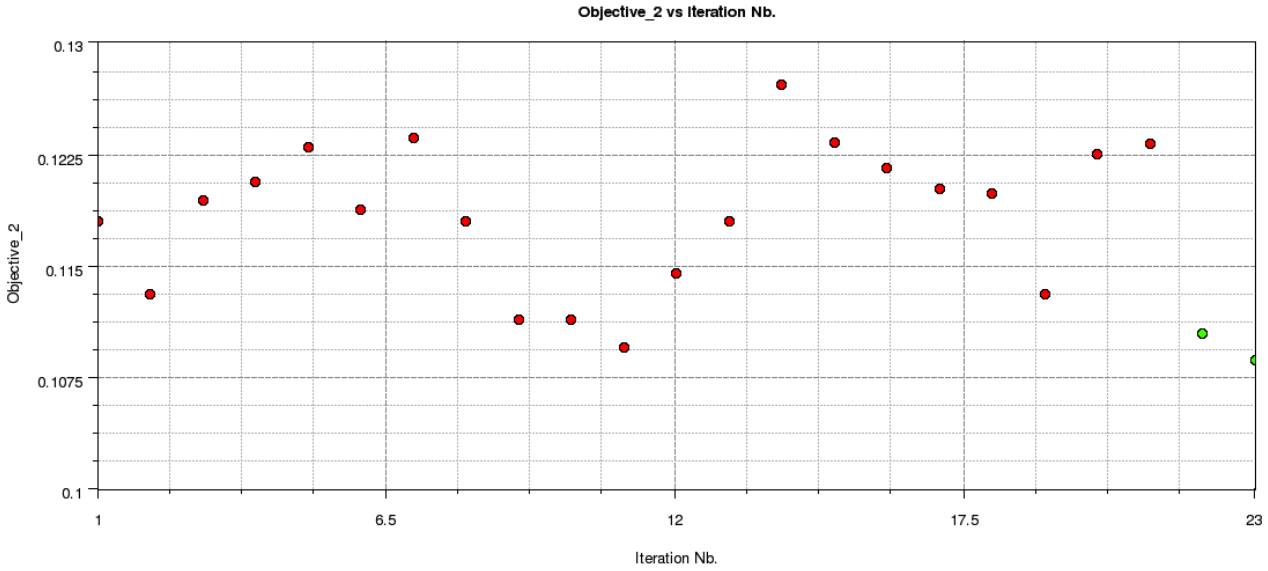

Figure 4.3.7: *The applied displacement (in [m]) when delamination initiation occur (i.e. the optimization objective) as a function of the iteration number for the optimization starting from a layup with all plies oriented in the [0/90] direction. The green circles indicate that the constraint conditions are satisfied.*

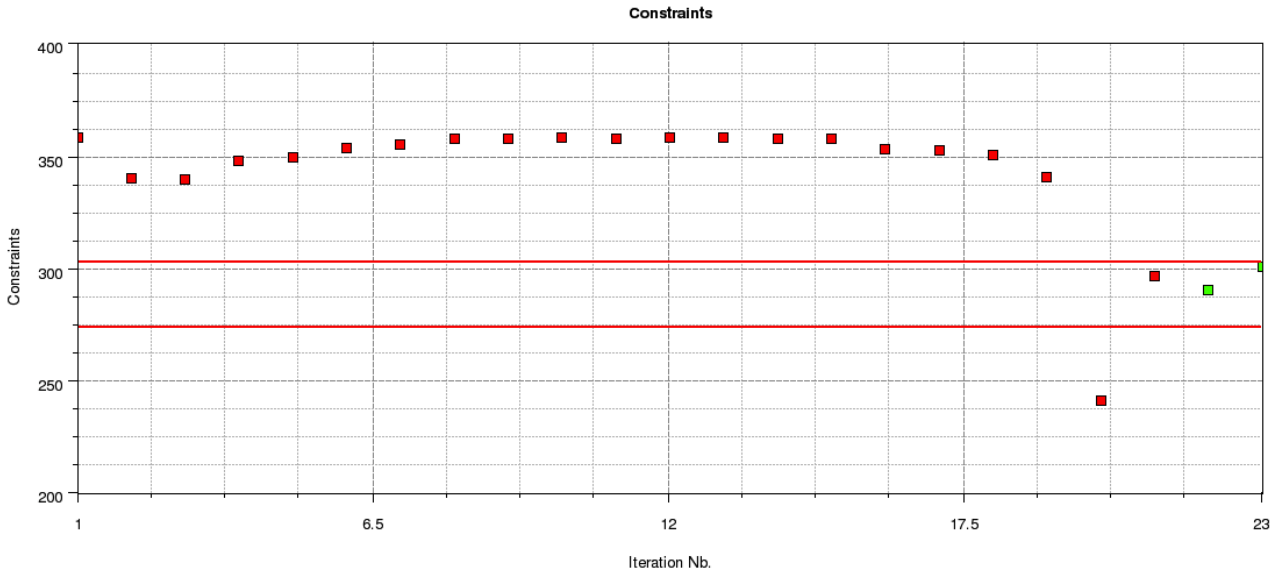

Figure 4.3.8: *The stiffness as function of the iteration number for the optimization starting from a layup with all plies oriented in the [0/90] direction. The two red lines represents the upper and lower boundary for the constraint corresponding to a 5% divergence from the stiffness of the original layup*

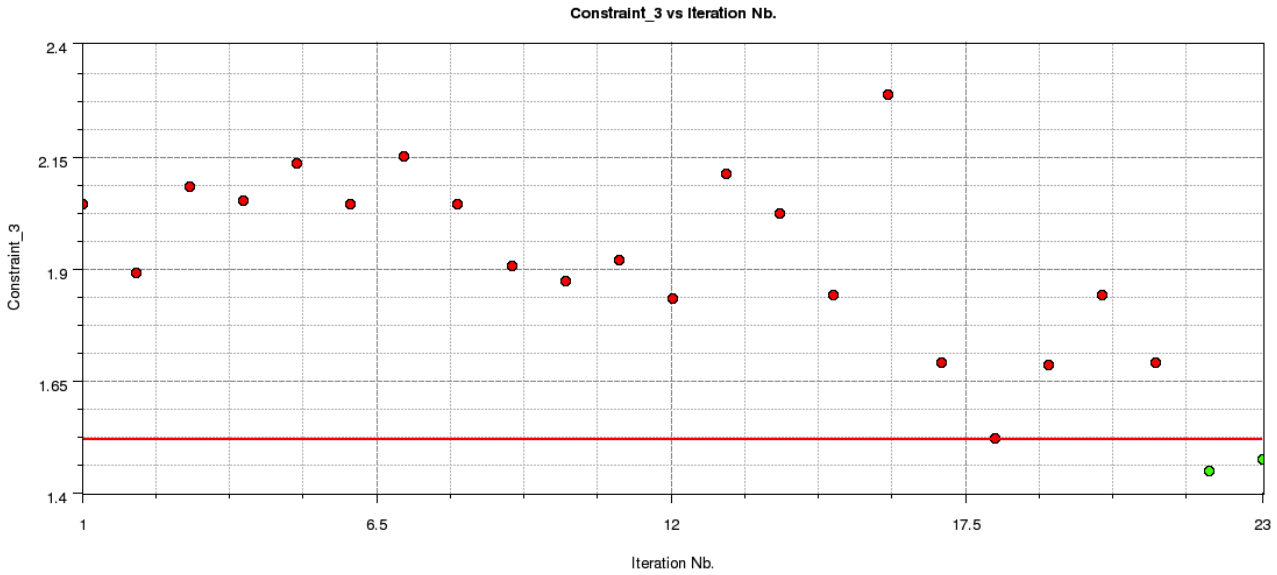

Figure 4.3.9: *The Tsai-Wu value as function of the iteration number for the optimization starting from a layup with all plies oriented in the [0/90] direction. The red line represents the value of the original layup which should not be exceeded.*

Table 4.3.2: Results from the optimization starting from a layup with all plies oriented in the [0/90] direction.

Layup	Fiber angle for ply #																		Stiff.	Tsai-Wu	Disp.
	01	02	03	04	05	06	07	08	09	10	11	12	13	14	15	16	17	18	$[N/m]$	-	$[m]$
Original	45	0	45	0	45	0	45	0	45	0	45	0	45	0	45	0	45	0	2885	1.512	0.1262
Optimal	0	45	0	45	0	0	0	0	0	0	0	0	45	45	0	45	45	0	2904	1.451	0.1104

Another thing that could be observed from these results is how the ply angles affect the stiffness of the spring in the orthosis. When all plies are oriented in the [0/90] direction the spring becomes much stiffer as can be seen in Table 4.3.3. When all plies instead are oriented in the [±45] the spring becomes less than half as stiff as the original layup.

Table 4.3.3: The stiffness of the spring with the original layup and with layups with all plies oriented [0/90] and [±45].

Layup	**Relative stiffness**
Original	1
$[0/90]_{18}$	1.24
$[\pm 45]_{18}$	0.40

5 Conclusions and discussion

5.1 Delamination modeling

The results from the delamination modeling are considered to have fulfilled the expectations. The modeled load-displacements curves are generally in very good agreement with the theoretical curves. For the DCB- and ENF test the curves, including the loads to delamination propagation, coincide very well with the theoretical ones. The result are also in good agreement with experiments, cf. [7]. The mixed mode (FRMM) test did not show as good agreement with the theoretical values as the previous cases but the results are reasonable. The tendency of the load -displacement relation could be captured even though the load levels were a bit overestimated. It is difficult to know what caused this smaller disagreement. One possible reason is that the mesh was too coarse. A finer mesh was used but the solution never converged. This also showed that it is much harder to achieve accurate modeling results for the case with a load resulting in a combination of the different basic modes which normally is the case in the reality.

Other than showing that it is possible to model basic delamination modes in an accurate way this part also served to get an understanding of how to perform the modeling. For example valuable knowledge was gained about which element types to use, how to specify the cohesive behavior and how to choose a proper element size.

5.2 Four-point bending test

The results from Four-point bending test are also considered successful even though the delamination process, which could be noted in the failed test specimens, could not be captured. The failure of the test specimen is a very complex event and to be able to properly capture the entire failure procedure was maybe to expect too much. It is far from obvious what occurs in the specimen after the compressive failure of the top ply. Probably failure modes such as micro buckling of the fibers are present which makes the modeling difficult. However, the models using the Hashin criteria worked very well to estimate the force causing the top ply to fail and also causing complete failure. To study the delamination process it would probably have been better to simulate inter-laminar shear strength (ILSS) test that it later turned out that SP had performed for two specimens of the same material as the orthosis. This way it also could have been possible to obtain fracture energies and interface strengths adjusted for the composite used in the orthosis.

Another thing learned from this modeling is that the properties of the specimens vary a lot depending of how they are manufactured. Large differences were found between the test specimens made by the different orthopedic engineers. The main reason for this is probably that different pressures have been applied when pressing the plies together which causes different fiber volume and matrix volume ratios in the specimens. Not knowing the amount of fiber contents in the specimens make the modeling very uncertain. It is also very possible that other manufacturing defects, such as for example voids between the plies, exist in the test specimens which also causes the results to differ from the theoretical ones.

5.3 Orthosis - ply orientation optimization

The modeling of the orthosis was successful in the way that initiation of delamination could be predicted in the heel area. Unfortunately, the optimization study did not result in any extensive improvement of the lay-up orientations in order to prevent delamination initiation. One reason why the optimization did not give as good results as expected is probably that the limits of the stiffness were set to narrow. From the results it could be seen that just changing one ply direction sometimes was enough to exceed the limit of 5% deviation. It can also be discussed whether or not it is a good method to study the delamination initiation by letting the analysis stop when it encounters convergence problem. It was assumed that the convergence problems occurred just after the point of delamination initiation. This is a bit unstable and an uncertain method since it is possible that the analysis manage to take some more time steps. It is also possible that convergence problems occur for other reasons than delamination initiation in the heel area, e.g. due to problems in the area where the displacement is applied. This may be the reason of why some irregularities were found in the optimization curves. To avoid problems like this, a script that checked whether or not the the delamination initiation parameter was fulfilled for the heel area could be written. Unfortunately, such a script was never implemented successfully in this

thesis work. Another element of uncertainty with this kind of method is the length of the time step. To achieve good results it is important to choose a sufficiently small time step. In the same time it is desirable to use quite long time steps to keep the computing times at a reasonable level. It is possible that the desire to keep down the computing times may have affected the results slightly in this study. To decrease the computing times a quite large mesh was used and it is possible that also this may have caused inaccuracies in the results. The quality of the mesh was neither perfect, narrow elements with sharp corners could not be avoided since the seed curves for the draping of the plies needed to be followed. Moreover, the optimization method used was probably not very appropriate for this kind of optimization problem with a lot of different design variables that only could take on two discrete values. If more time had been available it would have been interesting to see which results that would have been obtained if the design variables, i.e. the ply orientation angles, had been set to take on more than two values. Unfortunately this is a very time consuming thing to do (regarding the computing time) and it would then have been necessary to introduce other restrictions for the design variables. It would also have been interesting to use a genetic optimization algorithm instead of the used ARSM method. This method follows Darwin's principle of survival of the fittest and is designed for problems like this having many design variables that only could take on two discrete values. More information about this can be found in [9]. Another option instead of performing the optimization study would have been to perform a so called Design of Experiment (DOE) study. In such a study, the effects of the design variables can be studied by running simulations with various combinations of parameter settings. This way it would have been possible to evaluate a couple of layups of interest in more detail.

As a final conclusion it can be said that the different ply layups do not seem to give any large effects on the delamination initiation behavior. According to the experience of the orthopedic engineers at Borås Hospital it is more difficult for cracks to propagate between layers oriented in [$\pm$45] direction. Unfortunately, this could not be verified in this analysis since only the initiation of the delamination was studied and not the propagation. However, the optimization study resulted in some knowledge in how the different ply angles affected the behavior of the orthosis regarding for example the stiffness. From the optimization study it could be seen that it was just the orientation of the outermost plies that affected the stiffness of the orthosis. The orientation of the six innermost plies had negligible effect on the stiffness. This indicates that it might be a good idea to have these plies oriented in [$\pm$45] direction. This way it could be harder for delaminations to propagate meanwhile the stiffness remains unchanged. At least, having all the inner plies orientated in the same direction ought to be a improvement since variation in the ply orientation is a causation to stress concentrations. Before focusing on optimize the ply angles, it might also be a good idea to first find a better and consistent manufacturing procedure which "always" results in a high quality product.

6 Future work

The focus in this thesis work has been to optimize the delamination failure performance of the orthosis by varying the ply orientation angles. This is only one of several ways to improve the design of the orthosis. Some recommendations of what can be investigated in a possible future work are:

- Change the geometry of the orthosis. For example the radius of the critical heel section could be increased to minimize the stresses.
- Change the material in the orthosis. One suggestion which have been considered is to substitute some of the carbon fiber plies with glass fiber plies.
- Change the ply stacking sequence of the orthosis.
- Change the number of plies in the different parts of the orthosis.

Some other things to be considered and which could be done in further analyses are:

- Simulate inter-laminar shear strength (ILSS) test to evaluate fracture energies and interface strengths for the composite used in the orthosis. SP has performed an ILSS test of two test specimens of the same material as the orthosis which can be used as a reference.
- Investigate the effect of the mesh size in the modeling of the orthosis. It is possible that inaccuracies in the results exist due to the fact that the mesh is not sufficiently fine.
- Test to let the design variables, i.e. the ply orientation angles, take on more discrete values in the optimization study.
- Test to use other optimization algorithms instead of the used ARSM method. Fore example a genetic optimization algorithm could be used. This method is designed for problems having many design variables that only could take on two discrete values and might therefore suit this problem better.

References

[1] Lunsford T.R., Ramm T, and Miller J.A. "Viscoelastic Properties of Plastic Pediatric AFOs." In: *Journal of Orthotists & Prosthetists* 6.1 (1994), pp. 3–9.

[2] Berge J and Lerneryd E. *Spring orthosis analysis. Finite element modelling and optimization of a composite material.* Master's Thesis 2010:40. Department of Applied Mechanics, Chalmers University of Technology, 2010.

[3] Sjogren A. *Haverianalys av springorthos.* As Manus Materialteknik AB, 2010.

[4] *Composite material.* 2011. URL: `http://en.wikipedia.org/wiki/Composite_material`.

[5] Cerioni A. *Simulation of delamination in composite materials under static and fatigue loading by cohesive zone models.* Doctor's Thesis. Department of Mechanical Engineering, University of Cagliari, 2009.

[6] *Abaqus Analysis User's Manual.* Version 6.11. Simulia, 2011.

[7] Hallett S.R. and Harper P.W. "Cohesive zone length in numerical simulations of composite delamination." In: *Enginering Fracture Mechanics* 75.16 (2008), pp. 4774–4792.

[8] Andre A, Nilsson S, and Asp L.E. "Finite Element Delamination Study of a Notched Composite Plate under Flexural Loads". In: *Journal of Materials Science and Engineering* 4.8 (2010), pp. 66–73.

[9] *HyperStudy 11.0 User Guide. Optimization.* Altair Engineering, Inc, 2011. URL: `http://www.altairhyperworks.com/hwhelp/Altair/hw11.0/help/mathsol/mathsol.aspx`.

[10] Burlayenko V.N. and Sadowski T. "FE modeling of delamination growth in interlaminar fracture specimens." In: *Budownictwo i Architektura* 2 (2008), pp. 95–109.

[11] *Composite Modeler for Abaqus Manual.* Version 1.0k. Simulayt, 2010.

[12] Demarco K, Reeder J.R., and Whitley K.S. "The use of doubler reinforcement in delamination toughness testing". In: *Composites Part A: Applied Science and Manufacturing* 35.11 (2004), pp. 1337–1344.

A Analytical solution for the benchmark delamination tests

For the three different test cases, described in section 3.1, investigating mode I-, mode II- and mixed mode delamination the analytical load-displacement relation could be calculated using corrected beam theory.

A.1 Mode I DCB test

Using simple beam theory the tip displacement, δ, of the DCB specimen (see Figure 3.1.1a) can be calculated as, cf. [7]

$$\delta = \frac{2Pa^3}{3E_1 I} \tag{A.1.1}$$

where P is the applied load, a is the crack length, E_1 is the longitudinal Young's modulus and I is the area moment of inertia for each cantilever. Given the width of the specimen, B, and the cantilever depth, h the area moment of inertia is calculated as

$$I = \frac{Bh^3}{12} \tag{A.1.2}$$

In this simplified beam theory the deflection due to shear deformations and deformations around the crack tip are neglected. To account for these deformations a correction parameter, χ, can be introduced into Equation A.1.1 which then becomes

$$\delta = \frac{2P(a+\chi h)^3}{3E_1 I} \tag{A.1.3}$$

where

$$\chi = \sqrt{\frac{E_1}{11G_{13}}\left[3 - 2\left(\frac{\Gamma}{1+\Gamma}\right)^2\right]} \tag{A.1.4}$$

and

$$\Gamma = 1.18\frac{\sqrt{E_1 E_2}}{G_{13}} \tag{A.1.5}$$

The strain energy release rate is given by, cf. [12]

$$G = \frac{P}{2B}\frac{d\delta}{da}\Big|_{P=const} \tag{A.1.6}$$

By substituting Equation A.1.3 into Equation A.1.6 the following expression for the mode I strain energy release rate is obtained

$$G_I = \frac{P^2(a+\chi h)^2}{BE_1 I} \tag{A.1.7}$$

When the strain energy release rate, G_I, is equal to the the critical value, G_{IC} the crack begins to propagate. After reaching this point the load-displacement relation is obtained by setting G_I equal to G_{IC} and combining Equation A.1.3 and A.1.7

A.2 Mode II 3ENF test

For the 3 point ENF specimen (see Figure 3.1.1b) the central displacement is, according to [7], given by

$$\delta = \frac{P[3(a+0.42\chi h)^3 + 2L^3]}{96E_1 I} \tag{A.2.1}$$

In this case the crack length correction term is $0.42\chi h$. In the same way as for the DCB-specimen the mode II strain energy release rate can be calculated by substituting this equation into Equation A.1.6 which gives

$$G_{II} = \frac{3P^2(a+0.42\chi h)^2}{64BE_1 I} \tag{A.2.2}$$

This equation can then, just as in the previous case, be used to find the load-displacement relation by combining it with the expression for the displacement.

A.3 Mixed-mode (FRMM) test

The tip displacement for the FRMM specimen (see Figure 3.1.1c) is calculated as, cf. [7]

$$\delta = \frac{P[7(a+0.42\chi h)^3 + (L+2\chi h)^3]}{24E_1 I} \tag{A.3.1}$$

In this case the values of the mode I and mode II energy release rates are given by

$$G_I = \frac{P^2(a+\chi h)^2}{4BE_1 I} \tag{A.3.2}$$

$$G_{II} = \frac{3P^2(a+0.42\chi h)^2}{16BE_1 I} \tag{A.3.3}$$

The analytical load-displacement could then be calculated by use of the failure criterions described in section 2.4. In this study the power law criterion was used with α set to one. For this case with a combination of only two failure modes it can be simplified to

$$\left(\frac{G_I}{G_{IC}}\right)^{\alpha} + \left(\frac{G_{II}}{G_{IIC}}\right)^{\alpha} = 1. \tag{A.3.4}$$

B Results from the 4-point bending test by SP

Table B.0.1: Results from the 4-point bending test by SP.

Specimen #	**Thickness [mm]**	**Max load [kN]**	**Max disp. [mm]**
1	5.58	5.30	20.5
2	5.28	4.39	21.6
3	5.60	4.80	18.0
4	5.30	4.75	23.9
5	5.18	4.40	24.2
6	5.19	4.35	26.9
7	4.78	4.05	27.5
8	4.73	4.17	26.4
9	4.78	3.99	29.2

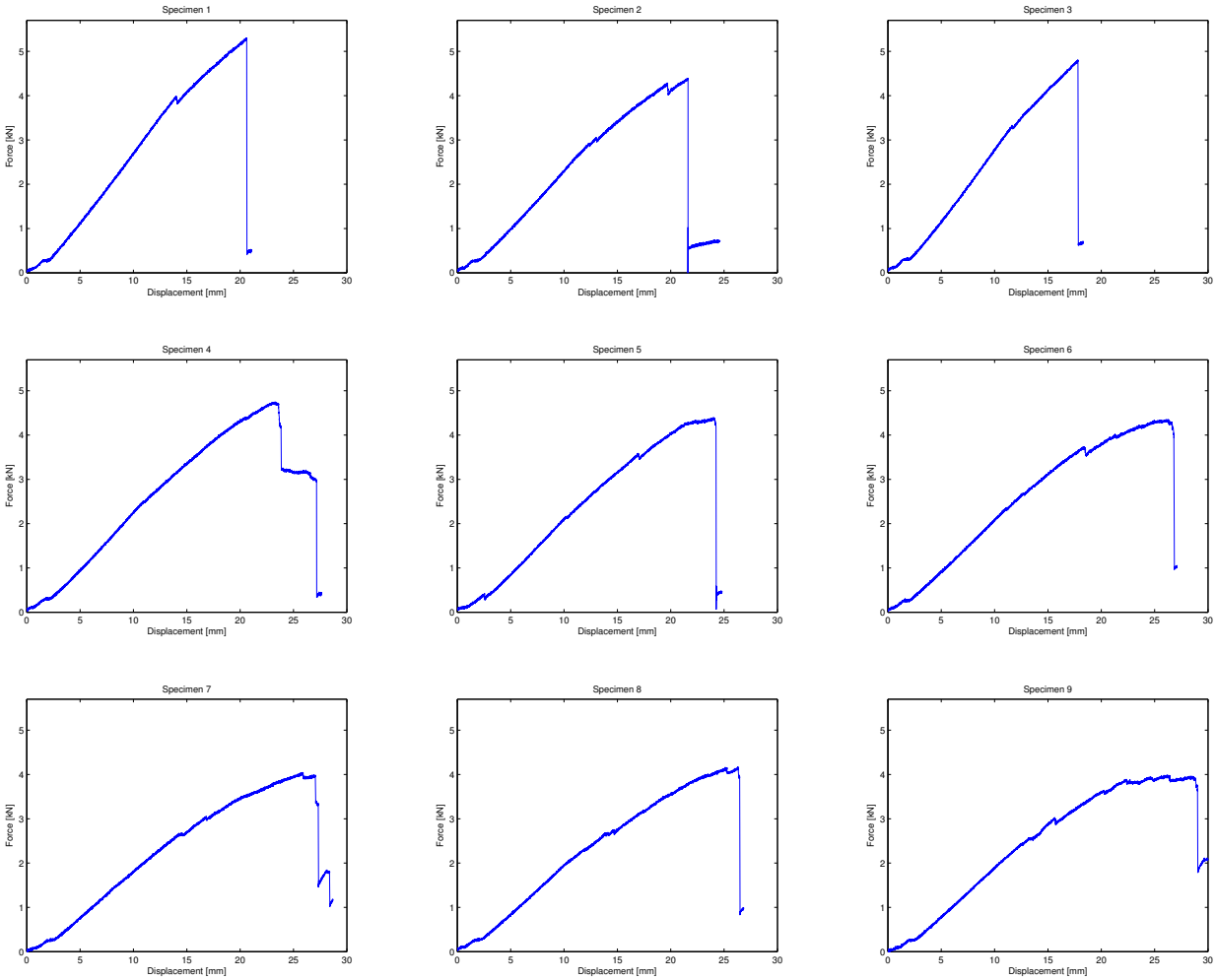

Figure B.0.1: *Force - displacement relations for the 4-point bending tests by SP.*

C Results from optimization

In Table C.0.1 and Table C.0.1 are the results from the ply angle layup optimizations presented. It should be clarified that a ply fiber angle of 0° means a [0/90] twill and a fiber angle of 45° a [±45] twill. The rows colored green indicate that the constraint conditions are fulfilled.

In the first table results are presented from the optimization starting from the original ply layup, where every second ply is oriented in the [0/90] direction and the rest [±45] . The second table shows the result when rom a layup with all plies oriented in the [0/90] direction.

Table C.0.1: Results from the optimization starting from the original ply layup.

Iteration	Fiber angle for ply #																		Stiffness [N/m]	Tsai-Wu	Displacement [m]
	01	02	03	04	05	06	07	08	09	10	11	12	13	14	15	16	17	18			
1	45	0	45	0	45	0	45	0	45	0	45	0	45	0	45	0	45	0	2885	1.512	0.1262
2	0	0	45	0	45	0	45	0	45	0	45	0	45	0	45	0	45	0	3161	1.288	0.1086
3	45	45	45	0	45	0	45	0	45	0	45	0	45	0	45	0	45	0	2547	1.427	0.1286
4	45	0	0	0	45	0	45	0	45	0	45	0	45	0	45	0	45	0	3061	1.448	0.1270
5	45	0	45	45	45	0	45	0	45	0	45	0	45	0	45	0	45	0	2710	1.596	0.1255
6	45	0	45	0	0	0	45	0	45	0	45	0	45	0	45	0	45	0	2989	1.499	0.1265
7	45	0	45	0	45	45	45	0	45	0	45	0	45	0	45	0	45	0	2815	1.564	0.1262
8	45	0	45	0	45	0	0	0	45	0	45	0	45	0	45	0	45	0	2921	1.517	0.1274
9	45	0	45	0	45	0	45	45	45	0	45	0	45	0	45	0	45	0	2869	1.593	0.1301
10	45	0	45	0	45	0	45	0	0	0	45	0	45	0	45	0	45	0	2899	1.507	0.1261
11	45	0	45	0	45	0	45	0	45	45	45	0	45	0	45	0	45	0	2881	1.520	0.1271
12	45	0	45	0	45	0	45	0	45	0	0	0	45	0	45	0	45	0	2905	1.503	0.1252
13	45	0	45	0	45	0	45	0	45	0	45	45	45	0	45	0	45	0	2858	1.502	0.1269
14	45	0	45	0	45	0	45	0	45	0	45	0	0	0	45	0	45	0	2928	1.532	0.1262
15	45	0	45	0	45	0	45	0	45	0	45	0	45	45	45	0	45	0	2792	1.548	0.1263
16	45	0	45	0	45	0	45	0	45	0	45	0	45	0	0	0	45	0	2965	1.548	0.1266
17	45	0	45	0	45	0	45	0	45	0	45	0	45	0	45	45	45	0	2704	1.688	0.1257
18	45	0	45	0	45	0	45	0	45	0	45	0	45	0	45	0	0	0	3025	1.791	0.1273
19	45	0	45	0	45	0	45	0	45	0	45	0	45	0	45	0	45	45	2548	1.455	0.1262
20	45	45	0	0	0	0	0	45	45	45	45	45	45	45	0	0	45	0	2895	1.379	0.1222
21	45	45	0	0	45	0	0	45	45	0	45	0	45	0	0	0	45	0	2902	1.419	0.1291
22	45	45	0	0	45	0	45	45	45	0	45	0	45	0	45	0	45	0	2778	1.447	0.1299

Table C.0.2: Results from the optimization starting from a layup with all plies oriented in the [0/90] direction.

Iteration	Fiber angle for ply #																		Stiffness [N/m]	Tsai-Wu	Displacement [m]
	01	02	03	04	05	06	07	08	09	10	11	12	13	14	15	16	17	18			
1	0	0	0	0	0	0	0	0	0	0	0	0	0	0	0	0	0	0	3581	2.058	0.1187
2	45	0	0	0	0	0	0	0	0	0	0	0	0	0	0	0	0	0	3397	1.890	0.1131
3	0	45	0	0	0	0	0	0	0	0	0	0	0	0	0	0	0	0	3395	2.175	0.1236
4	0	0	45	0	0	0	0	0	0	0	0	0	0	0	0	0	0	0	3476	2.051	0.1206
5	0	0	0	45	0	0	0	0	0	0	0	0	0	0	0	0	0	0	3491	2.133	0.1229
6	0	0	0	0	45	0	0	0	0	0	0	0	0	0	0	0	0	0	3530	2.043	0.1187
7	0	0	0	0	0	45	0	0	0	0	0	0	0	0	0	0	0	0	3550	2.148	0.1236
8	0	0	0	0	0	0	45	0	0	0	0	0	0	0	0	0	0	0	3572	2.043	0.1179
9	0	0	0	0	0	0	0	45	0	0	0	0	0	0	0	0	0	0	3574	1.905	0.1114
10	0	0	0	0	0	0	0	0	45	0	0	0	0	0	0	0	0	0	3577	1.873	0.1114
11	0	0	0	0	0	0	0	0	0	45	0	0	0	0	0	0	0	0	3572	1.919	0.1095
12	0	0	0	0	0	0	0	0	0	0	45	0	0	0	0	0	0	0	3577	1.834	0.1145
13	0	0	0	0	0	0	0	0	0	0	0	45	0	0	0	0	0	0	3578	2.143	0.1194
14	0	0	0	0	0	0	0	0	0	0	0	0	45	0	0	0	0	0	3572	2.022	0.1271
15	0	0	0	0	0	0	0	0	0	0	0	0	0	45	0	0	0	0	3572	1.835	0.1229
16	0	0	0	0	0	0	0	0	0	0	0	0	0	0	45	0	0	0	3527	2.286	0.1215
17	0	0	0	0	0	0	0	0	0	0	0	0	0	0	0	45	0	0	3521	1.691	0.1201
18	0	0	0	0	0	0	0	0	0	0	0	0	0	0	0	0	45	0	3501	1.523	0.1198
19	0	0	0	0	0	0	0	0	0	0	0	0	0	0	0	0	0	45	3403	1.686	0.1131
20	0	45	45	45	45	45	45	0	0	0	0	45	45	45	45	45	45	0	2409	1.841	0.1224
21	0	0	45	45	0	45	0	0	0	0	0	0	45	45	0	45	45	0	2964	1.691	0.1231
22	0	45	0	45	0	0	0	0	0	0	0	0	45	45	0	45	45	0	2904	1.451	0.1104
23	0	0	45	0	45	45	0	0	0	0	0	0	45	45	0	45	45	0	3004	1.475	0.1087

Table C.0.3: Results from the optimization starting from a layup with all plies oriented in the [0/90] direction without the Tsai-Wu constraint.

Iteration	Fiber angle for ply #																		Stiffness [N/m]	Tsai-Wu	Displacement [m]
	01	02	03	04	05	06	07	08	09	10	11	12	13	14	15	16	17	18			
1	0	0	0	0	0	0	0	0	0	0	0	0	0	0	0	0	0	0	3581	2.058	0.1187
2	45	0	0	0	0	0	0	0	0	0	0	0	0	0	0	0	0	0	3397	1.890	0.1131
3	0	45	0	0	0	0	0	0	0	0	0	0	0	0	0	0	0	0	3395	2.175	0.1236
4	0	0	45	0	0	0	0	0	0	0	0	0	0	0	0	0	0	0	3476	2.051	0.1206
5	0	0	0	45	0	0	0	0	0	0	0	0	0	0	0	0	0	0	3491	2.133	0.1229
6	0	0	0	0	45	0	0	0	0	0	0	0	0	0	0	0	0	0	3530	2.043	0.1187
7	0	0	0	0	0	45	0	0	0	0	0	0	0	0	0	0	0	0	3550	2.148	0.1236
8	0	0	0	0	0	0	45	0	0	0	0	0	0	0	0	0	0	0	3572	2.043	0.1179
9	0	0	0	0	0	0	0	45	0	0	0	0	0	0	0	0	0	0	3574	1.905	0.1114
10	0	0	0	0	0	0	0	0	45	0	0	0	0	0	0	0	0	0	3577	1.873	0.1114
11	0	0	0	0	0	0	0	0	0	45	0	0	0	0	0	0	0	0	3572	1.919	0.1095
12	0	0	0	0	0	0	0	0	0	0	45	0	0	0	0	0	0	0	3577	1.834	0.1145
13	0	0	0	0	0	0	0	0	0	0	0	45	0	0	0	0	0	0	3578	2.143	0.1194
14	0	0	0	0	0	0	0	0	0	0	0	0	45	0	0	0	0	0	3572	2.022	0.1271
15	0	0	0	0	0	0	0	0	0	0	0	0	0	45	0	0	0	0	3572	1.835	0.1229
16	0	0	0	0	0	0	0	0	0	0	0	0	0	0	45	0	0	0	3527	2.286	0.1215
17	0	0	0	0	0	0	0	0	0	0	0	0	0	0	0	45	0	0	3521	1.691	0.1201
18	0	0	0	0	0	0	0	0	0	0	0	0	0	0	0	0	45	0	3501	1.523	0.1198
19	0	0	0	0	0	0	0	0	0	0	0	0	0	0	0	0	0	45	3403	1.686	0.1131
20	0	45	45	45	45	45	0	0	0	0	0	45	45	45	45	45	45	0	2441	1.605	0.1087
21	0	45	0	45	0	45	0	0	0	0	0	0	45	0	45	0	0	0	3141	1.783	0.1097
22	0	45	45	0	0	45	0	0	0	0	0	0	45	45	0	0	45	0	3030	1.654	0.1244
23	0	45	45	45	0	45	0	0	0	0	0	0	45	45	0	0	0	0	3016	1.528	0.1104
24	0	45	0	0	0	45	0	0	0	0	0	0	45	45	45	45	45	0	2841	1.828	0.1237